

Germanium-based Metal-Semiconductor-Metal Photodetectors for 1.550 μm Optical Communication Wavelength

By

Salia Mirbaha, B. Eng.

A thesis submitted to the
Faculty of Graduate Studies and Research
in partial fulfilment of the requirements for the degree of

MASTER OF APPLIED SCIENCE

In Electrical Engineering

Ottawa-Carleton institute for Electrical Engineering

Department of Electronics

Faculty of Engineering

Carleton University

© Salia Mirbaha, Dec 2009



Library and Archives
Canada

Published Heritage
Branch

395 Wellington Street
Ottawa ON K1A 0N4
Canada

Bibliothèque et
Archives Canada

Direction du
Patrimoine de l'édition

395, rue Wellington
Ottawa ON K1A 0N4
Canada

Your file *Votre référence*
ISBN: 978-0-494-68645-4
Our file *Notre référence*
ISBN: 978-0-494-68645-4

NOTICE:

The author has granted a non-exclusive license allowing Library and Archives Canada to reproduce, publish, archive, preserve, conserve, communicate to the public by telecommunication or on the Internet, loan, distribute and sell theses worldwide, for commercial or non-commercial purposes, in microform, paper, electronic and/or any other formats.

The author retains copyright ownership and moral rights in this thesis. Neither the thesis nor substantial extracts from it may be printed or otherwise reproduced without the author's permission.

In compliance with the Canadian Privacy Act some supporting forms may have been removed from this thesis.

While these forms may be included in the document page count, their removal does not represent any loss of content from the thesis.

AVIS:

L'auteur a accordé une licence non exclusive permettant à la Bibliothèque et Archives Canada de reproduire, publier, archiver, sauvegarder, conserver, transmettre au public par télécommunication ou par l'Internet, prêter, distribuer et vendre des thèses partout dans le monde, à des fins commerciales ou autres, sur support microforme, papier, électronique et/ou autres formats.

L'auteur conserve la propriété du droit d'auteur et des droits moraux qui protègent cette thèse. Ni la thèse ni des extraits substantiels de celle-ci ne doivent être imprimés ou autrement reproduits sans son autorisation.

Conformément à la loi canadienne sur la protection de la vie privée, quelques formulaires secondaires ont été enlevés de cette thèse.

Bien que ces formulaires aient inclus dans la pagination, il n'y aura aucun contenu manquant.


Canada

The undersigned recommend to the Faculty of Graduate
Studies and Research acceptance of the thesis,

Germanium-based Metal-Semiconductor-Metal Photodetectors for 1.550 μm Optical Communication Wavelength

Submitted by Salia Mirbaha, B. Eng.

In partial fulfilment of the requirements for the degree of
Master of Applied Science in Electrical Engineering

Professor Q. J. Zhang
Chairman, Department of Electronics

Thesis Supervisor, Niall Tait

OCIECE

Department of Electronics

Carleton University

January, 2010

Acknowledgements

It is my pleasure to express my sincere appreciation to my thesis supervisor, Dr. Niall Tait, for his guidance, encouragement and support throughout this work. He provided me with the opportunity to do this research and he was always willing to provide knowledge, expertise, and assistance. His professional and personal attitudes have made my stay at Carleton University a very rewarding and memorable experience.

I would like to extend my appreciation to Dr. N. Garry Tarr for his valuable guidance and Dr. Steven McGarry for his great help especially in optical measurement set up.

I am grateful to Rob Vandusen, Carol Adams, and Rick Adams for their support, training, and help with preparing samples in the microfabrication laboratory of Carleton University. Thanks should also be given to group IV staff specially Bonnie Brown, Janet Driver, and Joe Hempinstall for helping me in the fabrication lab.

I owe many thanks to my father, my mother, and my sister for their encouragement and support that enabled me to complete my thesis.

I would also like to thank all of my friends for their care, and being so great and supportive.

Abstract

Interdigitated Metal-Germanium-Metal photodiodes with Al as the Schottky barrier metal were fabricated using RF sputter deposition technique to deposit Ge. A variety of system parameters including growth temperature, RF power, and plasma hydrogen concentration were investigated for highest film quality and detector performance. Furthermore, modifications on the structure of the interdigitated MSM (Metal-Semiconductor-Metal) detectors that involves different width and spacing of electrodes, area size, as well as a novel design of semiconductor-on-metal for reducing surface effects has been pursued.

The device with highest current ratio gave responsivity of 2mA/W and dark current of $11.6\mu\text{A}$ at 5 volts for device area of $95\mu\text{m}$ by $110\mu\text{m}$. Highest responsivity achieved in this project was 2.5mA/W at 5 volts for device area of $100\mu\text{m}$ by $100\mu\text{m}$, however the dark current of this device was $170\mu\text{A}$, being the highest dark current among other samples.

Table of Contents

Acknowledgements.....	iii
Abstract.....	iv
Table of Contents.....	v
List of figures.....	viii
List of tables.....	xi
1 Introduction	1
1.1 Background	1
1.1.1 Optical communication.....	1
1.1.2 Materials for photodetectors	2
1.1.3 Review on Photodetectors.....	5
1.2 Thesis contributions	9
1.2.1 Metal-Germanium-Metal photodiodes.....	10
1.3 Thesis outline	10
2 Material choice of MSM photodetectors	11
2.1 Active layer	11
2.1.1 Polycrystalline semiconductors	11
2.1.1.1 Electrical and optical properties of polycrystalline semiconductors.....	12
2.1.2 Amorphous material.....	15
2.1.2.1 Transport in amorphous material	16
2.1.2.2 Hydrogenation effects	19
2.2 Contact metal.....	20
3 Theoretical concepts of MSM photodetectors.....	21
3.1 Metal-Semiconductor junction.....	21
3.1.1 Schottky contact.....	21
3.1.2 Current transport process	25
3.1.3 Depletion layer characteristic	28
3.1.3.1 Width and electric field.....	28
3.1.3.2 Junction capacitance.....	28
3.1.4 Ohmic contact	29

3.2	MSM theory	30
3.2.1	Dark current	31
3.2.2	Barrier height / Saturation current / Quality factor	36
3.2.3	Responsivity.....	37
3.2.4	Capacitance	39
3.2.4.1	Capacitance vs. Bias voltage.....	40
3.2.5	Detectivity.....	41
4	Material investigation, fabrication, and characterization	43
4.1	Choice of sputter deposition.....	43
4.2	Review of sputtered Ge thin films.....	44
4.3	System parameters and characterization of sputter deposited Ge films.....	47
4.3.1	X-ray diffraction	48
4.3.2	Resistivity	50
4.4	Conclusion.....	51
5	MSM photodetector fabrication and characterization	52
5.1	Fabrication.....	52
5.1.1	Substrate preparation; oxide on Si	52
5.1.2	C-V dots	52
5.1.3	Interdigitated MSM structures	54
5.1.3.1	Metal on semiconductor	54
5.1.3.2	Semiconductor on metal.....	56
5.2	Characterization	61
5.2.1	Dark current	61
5.2.1.1	C-V dots	61
5.2.1.2	Metal electrode effects	62
5.2.1.3	Interdigitated electrodes	65
5.2.1.4	Hydrogenation effects	69
5.2.2	Photoresponse	70
5.2.2.1	Metal on semiconductor	72
5.2.2.2	Semiconductor on metal.....	73
5.2.2.3	Hydrogenation effects	76

5.3	Conclusion.....	77
6	Conclusion and recommendations.....	78
6.1	Conclusion.....	78
6.2	Recommendations and future work.....	80
	References.....	81

List of figures

Figure 1.1 - Spectral response of different photodetector material [3].....	3
Figure 2.1- Schematic band diagram of the polycrystalline semiconductor with a periodic array of negatively charged grain boundaries [39].	13
Figure 2.2- The barrier height as a function of the dopant concentration for polysilicon [40]	13
Figure 2.3- Grain boundary barrier and parabolic barriers in polysilicon [40]	14
Figure 2.4- Schematic density of states distribution for an amorphous semiconductor showing the band tails and defect states between the conduction and valence bands	15
Figure 2.5-Illustration of three main conduction mechanisms in amorphous material	17
Figure 2.6 -Time resolved photoconductance of a-Si:H (a) Linear scale (b) Log-log scale [44]	18
Figure 3.1-Energy band diagram before contact [41].....	22
Figure 3.2- Energy band diagram after contact [41].....	23
Figure 3.3 - Ideal energy band diagrams of (a) Forward (b) Reverse bias [41]	24
Figure 3.4- Top and cross section view of MSM interdigitated photodiodes.....	31
Figure 3.5- (a) Schematic diagram (b) Energy band diagram of MSM structure [53]	32
Figure 3.6 - Potential profile of MSM detector after applying a bias voltage [53]	33
Figure 3.7-(a) Condition of reach-through voltage (b) Flat band condition (c) $V > V_{FB}$ [53]..	34
Figure 3.8-Theoretical I-V characteristics for a Si symmetric MSM with $N_D = 4 \times 10^{16} \text{ cm}^{-3}$ and $L = 12 \mu\text{m}$ at 300°K where Case (1) : $\phi_{n1} = 0.85\text{V}$ and $\phi_{p2} = 0.2\text{v}$; Case (2) : $\phi_{n1} = 0.85\text{V}$ and $\phi_{p2} = 1\text{v}$ [53].....	35
Figure 3.9-Capacitance versus side length of MSM and pin Photodetectors [55].....	39
Figure 3.10- Capacitance voltage characteristics of MSM detector [53]	41
Figure 4.1 – Example of an RF sputtering system [57]	44

Figure 4.2- Xray diffraction results of sample 1 (250°C) and sample 2 (450°C)	49
Figure 5.1- Picture of the CV dots with the probes on each dot.....	53
Figure 5.2- Photographs of 2.5 μm width and spacing MSM photodetectors	54
Figure 5.3- Cross section of the MSM interdigitated electrode (Metal above Ge).....	55
Figure 5.4- Mask design of second structure	57
Figure 5.5- Cross section of the second MSM interdigitated electrode design (Ge above metal electrodes)	59
Figure 5.6 – Picture of the fabricated sensors on the same chip.....	59
Figure 5.7- I-V characteristics of Sample 3, 4, 5, 8, 9, and 10	61
Figure 5.8- I-V Characteristics of metal on Single crystalline Ge samples.....	63
Figure 5.9- Logarithmic plot of $I \exp(qV/kT) \exp(qV/kT) - 1$ versus V of sample 6 at 293K	64
Figure 5.10- Sample 13 interdigitated electrode I-V characteristics for 5u, and 10u width/spacing electrodes	65
Figure 5.11- I-V characteristics of MSM photodiode with Cr metallization and 50u width and spacing (a) Dark current with different substrates (b) photocurrent of $\text{SiO}_2/\text{a-Si:H}/\text{p-Si}$ at different ranges of power [54]	66
Figure 5.12- I-V characteristics of $\text{SiO}_2/\text{n-Si}$ MSM photodiode with Pd metallization and 4u width and spacing (a)Dark current at different temperatures (b) photocurrent at 227°k [54]	67
Figure 5.13 – Barrier height VS leakage current of devices with same electrode area size (95 μm ×110 μm).....	68
Figure 5.14- Dark current at different hydrogen concentrations	70
Figure 5.15- Optical response measurement set up	71
Figure 5.16 – Transient response of sample 12	72

Figure 5.17- Photoresponse of sample 15(a), 21(b), 17(c), and 19(d).....73
Figure 5.18-Photocurrent at different hydrogen concentrations76

List of tables

Table 1.1- Important photodetector material at 300K [2].....	2
Table 2.1 - Features of atomic structure and the resulting electronic properties [42]	16
Table 4.1- Deposition conditions of samples prepared in [61].....	45
Table 4.2- Ar pressure vs. p to n conversion power [61].....	45
Table 4.3- Samples deposited under different system parameters.....	48
Table 4.4-Resistivity of different samples	50
Table 5.1 - Photodetector sample descriptions	60
Table 5.2- Ideality factor and dark current of the interdigitated MSM photodetectors.....	67
Table 5.3- Photoresponse of the sensors with different hydrogen concentration.....	74

Chapter1

Introduction

1.1 Background

1.1.1 Optical communication

Optical communication frequencies accommodate an increase in bandwidth of five to six orders of magnitude compared to RF frequencies. Optical communication in free space offers thousands of communication channels for both voice and data transmission. Much of the technology to meet the ultrawide bandwidth requirement has been developed for military and space communication programs, including the fiber optic telecommunications systems.

NIR (Near Infrared) is most commonly used with reference to wavelength between 0.7 and 2.0 μm . This part of IR is important in several applications, first among them are the optical communications with transmission wavelength located at favourable 1.3, and 1.55 μm that correspond to lowest signal attenuation and lowest chromatic dispersion in optical fibers respectively. 1.55 μm is widely used in optical transmission and this thesis focuses on transmission at this wavelength.

Optoelectronic integrated circuits offer the fabrication of electronics and optoelectronics in the same process that will considerably reduce interconnection and alignment problems, improving reliability, yield, and compactness [1]. Photodetectors are important optical electrical components in optic-electronic systems and there has been a lot of research done on them in order to monolithically integrate them with electronics. This work is focused on an MSM integrated photodetector sensor that is commonly integrated in electronics for its ease of

fabrication. The original motivation of this thesis was to investigate IR photodetectors for integration with Si and SOI MEMS micro-mirrors used in WSS (Wavelength Selective Switches). When the power incident on the micro-mirror gets to high, it can deform or damage surface of the micro-mirror. Therefore, existence of a photodetector was mandatory to monitor the power incident on the mirror, preventing it to reach its damaging thresholds. This work investigates an integrated photodetector with a fabrication process compatible with a MEMS micro-mirror process. This involved investigation of different material and structures of MSM detectors leading to different device performance and characteristics. Although this work focuses on only fabricating the photodetector, integrating two photodetectors on the sides of the mirror is thought to be the best possible approach for integrating a photodetector with the MEMS micro-mirror. In the next two sections, material choice and different photodetectors and their applications will be discussed.

1.1.2 Materials for photodetectors

Photodetectors are made from different semiconductor materials such as Silicon, Germanium, Indium-Gallium-Arsenide, and some other materials that are prominent materials used in photodetectors. Each material has a characteristic bandgap energy E_g , which determines its light-absorbing capabilities. Table 1.1 summarizes some of these materials with their cut-off wavelength, bandgap energy, and operating bandwidth [2].

Type	E_g (eV)	λ_c (nm)	Band
Silicon	1.12	1100	Visible
Gallium arsenide	1.42	875	Visible
Germanium	0.66	1800	Near-infrared
Indium gallium arsenide	0.73-0.47	1700 – 2600	Near-infrared
Indium arsenide	0.36	3400	Near-infrared

Table 1.1- Important photodetector material at 300K [2]

The equation between bandgap energy (E_g) and cut-off wavelength (λ_c) is [2]:

$$\lambda_c = \frac{1.24 \times 10^3 \text{ nm}}{E_g (\text{ev})}$$

That shows the smaller the bandgap is the higher the cutoff wavelength will be. From above equation, it can be found that for 1550 nm light detection, the maximum allowed band gap is 0.8ev, meaning that for band-gaps higher than 0.8ev, a photon is not able to move electron energy from valence band to conduction band and therefore there will not be any photocurrent generated.

Figure 1.1 shows measured responsivity (\mathfrak{R}) values of photodiodes with an absorption layer of Si, Ge and InGaAs vs. the operating wavelength [3].

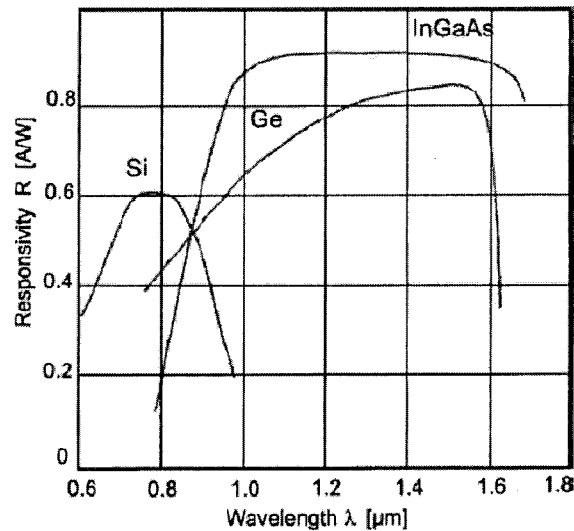


Figure 1.1 - Spectral response of different photodetector material [3]

As can be seen, silicon is a poor detector in the range of 1300 and 1550nm. Ion implantation of silicon [4], hydrogenating amorphous silicon, and SiGe heterojunctions are some of the alternatives to improve silicon absorption for optical communication.

SiGe heterojunction detector material is one approach to improve the performance of Silicon. SiGe-based optoelectronics provides a compromise between material performance and monolithic integration [1]. However the 4% lattice mismatch between Si and Ge in this material generates a high density of dislocations that will reduce life time by acting as carrier recombination and trapping states. $\text{Si}_x\text{Ge}_{1-x}$ layer is one of the solutions to the lattice mismatch between Si and Ge. This layer adjusts lattice through compression (in the growth plane) and tensile strain (along the normal) [1]. However with the $\text{Si}_x\text{Ge}_{1-x}$ layer there will still be a considerable amount of dislocation density that depends on Ge mole fraction. Using thin lightly doped SiGe layers (lower than critical thickness¹) can lead to unstrained Ge layers and therefore no dislocation density will be presented in the film. However this will lead to low quantum efficiency since for high light absorption, thick Ge layers are required. For example, with the results of Ge mole fraction vs. Critical layer thickness from Bean's model [1], and Ge mole fraction vs. Absorption coefficient [5], it can be found that for a $\text{Si}_{80\%}\text{Ge}_{20\%}$ at $1.30\mu\text{m}$, critical thickness is 200nm while absorbing 90% of light needs 1mm of Ge thickness. The use of pure Ge on Si was first attempted by Luryi *et al.* [6]. They first suggested using highly doped Ge layer with the same conductivity as Silicon in order to minimize dark/leakage current (current measured in the dark with no light illumination) and trapping states.

Ge is another promising material in optical communication because of its higher carrier mobility and lower bandgap that leads to higher optical absorption and faster response. However it produces higher leakage current due to the lower bandgap. Amorphous material like a-Si:H and a-Ge:H are good material for photodetection since they have larger optical absorption compared to crystalline Si and Ge. That is because in amorphous material the energy states within the

¹ Critical thickness is the thickness where the strain due to lattice mismatch reaches a threshold and film relaxation takes place

bandgap can capture lower energy photons and therefore increase the absorption coefficient compared to crystalline material. However due to these states, life time of the carriers are lower compared to crystalline material. Hydrogenation can help to increase life time of carriers by reducing the energy states within the forbidden bandgap area. Hydrogenated amorphous germanium is a natural candidate to substitute for hydrogenated amorphous silicon in applications requiring a material with small optical gap, such as in tandem solar cells or infrared detectors [7].

III-V compound semiconductors materials are another approach for photodetection. They show excellent characteristics on speed and quantum efficiency of the photodetectors. InGaAs for example is a widely used material for telecommunication at 1550 nm wavelength because of its 0.8eV bandgap, however these materials are not easily integrated with silicon and the process associated with their fabrication is complex, highly precise, and expensive.

1.1.3 Review on Photodetectors

The fundamental purpose of any photodetector is to convert optical signals into electrical signals, usually expressed as a photocurrent, which can be amplified, displayed and/or retransmitted. Various types of photodetectors have been extensively studied for a long time, including photoconductive, avalanche, Schottky barrier, p-n junction, p-i-n junction, phototransitive, and metal-semiconductor-metal (MSM) photodetectors [8].

One advantage of the MSM-PD structure is its relative ease of fabrication. One difficulty that is encountered in the fabrication of MSM-PDs for low-noise applications is that some of the

materials needed for photodetection have very small Schottky barrier heights with most metals, as with conventional schottky diode-based detectors [9].

Sugeta et al. first proposed and demonstrated the MSM photodetector in 1979 [10], then other MSM photodetectors were reported by Slayman and Figueroa [11], and by Wei et al in 1981 [12]. Since then there have been attempts to improve the performance of the diode by dark current reduction, speed and sensitivity optimization. Electrode asymmetry is considered as one of the ways of reducing the dark current. In [13] MSM photodetectors of Au/Ti on p-type silicon with two asymmetric electrodes have been reported. They show that by increasing the asymmetry of the metal electrodes, the leakage current decreases. They are however working at wavelength of 623nm and the results are not comparable to the detectors working at optical communication wavelength of 1550 nm. The same group report on using different metal electrodes in order to reduce the leakage current [14]. They have fabricated devices with different metal electrodes of Ni-Ge-Ti, Ni-Si-Ti, and other metals on p-type Si substrate and n-type Ge substrate with doping density of 10^{15} and 10^{16} cm^{-3} respectively. Devices with different metal electrodes show lower leakage current; however this method needs one more mask and adds to the fabrication processing. Antireflection coating [15] and surface passivation, are other approaches to dark current reduction that help to passivate the surface, and reduce the surface states using materials like oxide [16], SiO_2 [17], sulphur passivation [18], and polyimide passivation [19]. Including a Schottky barrier enhancement layer in between the metal and active layer is another approach for reducing the dark current of MSM photodetectors by increasing the Schottky barrier height of the metal semiconductor junction. J. Oh *et al.* [20] has reported on an amorphous Ge layer of 50 nm between Ag metal and an UHV-CVD deposited Ge on Si substrate. They have shown than enhancing the amorphous layer decreases the dark current by

two orders of magnitude, being $7.5 \mu\text{A}$ at 3 V. Their device has responsivity of 0.15A/W (QE of 14.3%) @ $1.3\mu\text{m}$, however the external quantum efficiency of their device falls down to 2.5% based on their graphs and therefore leading to responsivity of about 0.031A/W @ $1.550 \mu\text{m}$. Furthermore, UHV-CVD is an expensive deposition (trade-off with low price) process compared to sputter deposition or evaporation deposition techniques which makes their device processing more expensive. Dopant segregation was proposed for high performance schottky source/drain MOSFETs by Kinoshita *et al* [21]. H. Zang and S.J. Lee [22] have shown for the first time the application of dopant segregation for dark current suppression, in metal-germanium-metal photodetectors. They were able to reduce the dark current by 3 to 4 orders of magnitude by dopant segregating the contact to have the dark current of 10^{-7} A and responsivity of 0.12A/W at -1v @ $1.550 \mu\text{m}$. Having NiGe as the contact metal because of its low resistivity, two step Ge growth [23][24], and also the dopant segregation, increases the complexity of the design. This group also reports on the same device structure but with Sulfur co-implantation and segregation [25].

In applications that high responsivity is needed, depending on the wavelength of operation, and absorbing layer material, thickness of the absorbing layer to absorb most of the light can be so high that it degrades speed of the device, and therefore the responsivity and speed of the MSM-PDs can be in a sever trade-off. For example, when operating at 830nm, Si needs about $12\mu\text{m}$ to absorb all the light. Henry *et al.* [26] have proposed an MSM-PD with $5\mu\text{m}$ silicon membrane. The basic concept of their device is to ensure that the carriers are generated in high field region while the back surface scatters the light within the membrane, causing light trapping. This device has shown a 3dB bandwidth of 3GHz and responsivity of 0.17A/W at 10v @ $830\mu\text{m}$, however the texture at the back surface complicates the design and increases the cost. Ho *et al.* [27] have

suggested a device based on the same concept as [26], but with trench electrodes that remove the back side polish and etch. This device shows 3dB bandwidth of 2.2 GHz at 5v and responsivity of 0.14A/W at 5V @ 790nm, however the metal electrodes (TiW-Au), can't be uniformly deposited because of the vertical structure of the trench electrodes. Laih et al. [28] further improved this design by having the electrodes to be in a V shape and therefore more uniform metal layer deposition. However both of the former designs have one more mask because of the trench electrodes.

Metal-Germanium-Metal photodetectors are of interest because of Germanium's compatibility with Si IC technology, higher mobility, and higher absorption coefficient at 1.550 μm as already mentioned in the previous section. D.Buca *et al.* [29] have demonstrated two different M-Ge-M designs. The first design is interdigitated Cr electrodes on MBE deposited Sb doped Ge on Si(111) of high resistivity substrate. This design shows fast response of 12.5ps FWHM and quantum efficiency of 7.5% @ 1.550 μm (Responsivity of 0.094 A/W). However, the high temperature involved in the cleaning process (800°C) places severe limitations on the integration of the detector. Their second design is MSM detectors with plate capacitor electrodes. They made a Cr/Ge/CoSi₂ heterostructure device, with FWHM of 9.4 ps, but their QE dropped down to 0.9% ($\mathfrak{R} = 0.011\text{A/W}$).

L. Colace *et al.* [30] have reported on MSM detectors based on epitaxial Ge /Si. Their device has responsivity of 0.24A/W at 1v @1.3 μm , but the LP-CVD deposition process makes the process more expensive. The same group have reported MSM photodetectors based on evaporated poly-Ge on Si [31]. This device shows responsivity of 16mA/W at 0.2 reverse bias@1.32 μm . A review of their works can be found in [32]. A polycrystalline Ge on Si heterojunction

photodetector has been also demonstrated by G. Masini [33] operating at $1.550\ \mu\text{m}$ with responsivity of 5mA/W and dark current of 1mA/cm^2 . Poly-Ge was thermally evaporated at a low temperature of 300°C which makes the device fully compatible with Si technology. MSM photodetectors of polycrystalline silicon have been investigated by R. P. MacDonald *et al.* [34] operating at 860nm . The bandwidth of 750MHz and responsivity of $0.13\ \text{A/W}$ shows a good performance of the device; however it cannot be compared to the devices operating at $1.550\ \mu\text{m}$ of optical communication wavelength. Recently K. W. Ang [35] have demonstrated an MSM Ge detector on a silicon waveguide with a Si:C schottky barrier enhancement. Their device has responsivity of 0.530A/W and dark current of 11.5nA at 1v bias @ $1.550\ \mu\text{m}$. However high temperature epitaxial growth and two step Ge deposition as well as the Si:C layer depositions makes the process of the device quite complicated. L. Vivien *et al.* [36] have shown an integrated MSM Ge photodetector in Si Rib waveguides with responsivity as high as $1\ \text{A/W}$, $150\ \mu\text{A}$ at 1v @ $1.550\ \mu\text{m}$. This high responsivity device shows higher dark current compared to the conventional MSM detectors and is specific for applications that the detector is integrated in the waveguide. Although the process steps are compatible with CMOS technology, there are too many process steps that complicate the design.

1.2 Thesis contributions

This project investigates NIR photodetectors for integration with Silicon and SOI MEMS. This requires Si process compatibility and low temperature processing. Sputtered Ge films are deposited at low temperatures and lower cost, being the motivation for using this technique for Si integration.

1.2.1 Metal-Germanium-Metal photodiodes

Germanium was investigated as the material of choice for MSM detector because of its higher absorption and higher mobility, and compatibility with Si technology initially. Metal-semiconductor-metal detectors were chosen as the photodetector sensing structure because of their ease of fabrication. Ge was sputter deposited, and it was found that a-Ge:H gave the lowest leakage current between other samples. It is the first time to the authors knowledge that a-Ge:H material is used as the sensing material for MSM-PD applications. Furthermore, a novel structure of Semiconductor-on-metal rather than the conventional metal-on-semiconductor have been introduced that reduces the leakage current density for more than a factor of 100. A sketch of the new proposed MSM structure is shown in Figure 5.5.

1.3 Thesis outline

This thesis describes a Metal-Ge-metal photodetector with different material and design modifications. Chapter 1 is an introduction on optoelectronics and integrated optics, as well as a review on MSM detector material and structures. Chapter 2 is on material choice for MSM-PDs including the governing theory of polycrystalline and amorphous semiconductors, while chapter 3 is an explanation of metal-semiconductor and MSM theory and their performance evaluation and characterization. Chapter 4 and chapter 5 provide information about the process, fabrication, characterization, and results of sputter deposited Ge films, and MSM detectors respectively. Chapter 6 is the conclusion chapter that also explains the future work of this project.

Chapter 2

Material choice of MSM photodetectors

2.1 Active layer

Conventional high performance III-V semiconductors have been the material of choice for photodetection applications. III-V compound materials however are not compatible with Si-based devices and are more expensive. Consequently group IV semiconductors have been alternatives for many optoelectronic components. Si in general has been the material of choice because of its lower cost and compatibility with Si ICs, but it lacks high absorption for long-haul communication wavelength photodetectors. Ge is also of interest for photodetection because of its lower bandgap, and higher mobility compared to Si, and compatibility with Si technology. Different Si and Ge crystal structures show different electrical and optical properties. The different properties of polycrystalline, single-crystalline, and amorphous Si and Ge can be related to the band structure of these materials that will be discussed in the following sections.

2.1.1 Polycrystalline semiconductors

A polycrystalline thin film is composed of crystallites¹ that are different in size and orientations. This variation can be caused by different growth conditions. Crystallites are joined by grain boundaries that are considered as defects in polycrystalline material. Polycrystalline material is usually deposited by chemical vapor deposition at temperatures of about 625°C, giving an average grain size of 70nm [37]. However chemical vapor deposition is a complex and

¹ Part of a solid-state material that has a structure of a single crystal

potentially expensive deposition process and sputtering or evaporation are alternative simpler processes. With sputtering however high quality crystalline thin films are not achievable and the films are generally amorphous. It has been reported that making sputter deposited crystallized Silicon is possible by introducing Al into Si [38]. Solid phase crystallization starting from amorphous layers is another method that can be used to obtain polycrystalline films. However this process is quite slow and requires about 20h at 600°C, but it can be reduced to a few minutes by rapid thermal annealing or by laser recrystallization with the grain sizes varying from 10nm to 1 μ m [39].

2.1.1.1 Electrical and optical properties of polycrystalline semiconductors

Grain boundaries in poly crystalline thin films bring out different electrical characteristics for polycrystalline thin films. The disordered atoms in grain boundaries can lead to dangling bonds in the material. These dangling bonds will allow some states within the bandgap of the semiconductor that are called traps in the bandgap. Electrons transferring in the thin film can get trapped by these states and therefore the properties of the film may change [40]. The electrical charge in the depletion regions forms a curved energy band as can be seen in Figure 2.1. This charge causes a potential barrier qV_B . V_B is the barrier height and is equal to:

$$V_B = \frac{qN_D}{2\epsilon_s} x_d^2 \quad (2.1)$$

Where q is the electronic charge, N_D is the dopant density, ϵ_s is the permittivity of Silicon and x_d is the width of the depletion region. When the polycrystalline film is lightly doped, most of the carriers can get trapped in the grains.

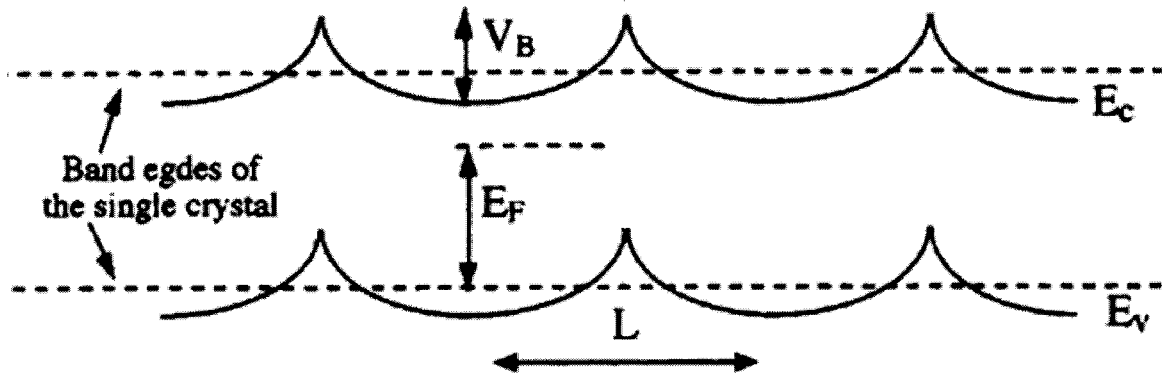


Figure 2.1- Schematic band diagram of the polycrystalline semiconductor with a periodic array of negatively charged grain boundaries [39].

As the doping increases more carriers will get trapped in the grain boundary until the dopant concentration reaches a critical value N^* ($N^* = N_T/L$). N_T is doping concentration, and L is grain boundary width. The carriers that do not get trapped by these states lead to a neutral region and cause the depletion region to shrink that is shown in Figure 2.2. As a result, with increasing the doping concentration, the barrier height first increases and then decreases after reaching N_T [41].

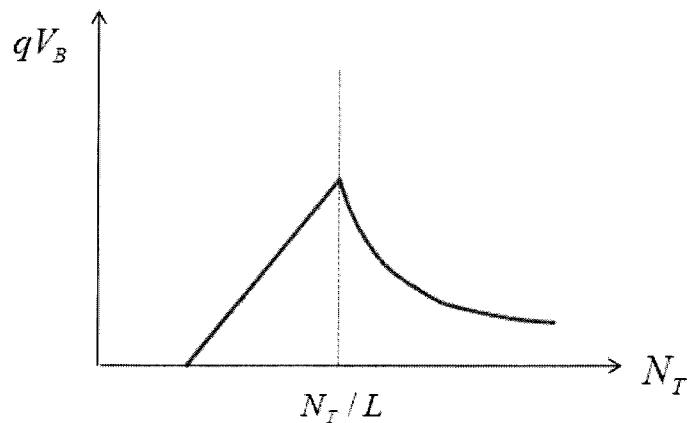


Figure 2.2- The barrier height as a function of the dopant concentration for polysilicon [40]

In addition to the parabolic depletion regions shown in Figure 2.1, the grain boundaries also affect the movement of electrons. This is modelled as a high narrow potential in the grain boundary that is shown in Figure 2.3.

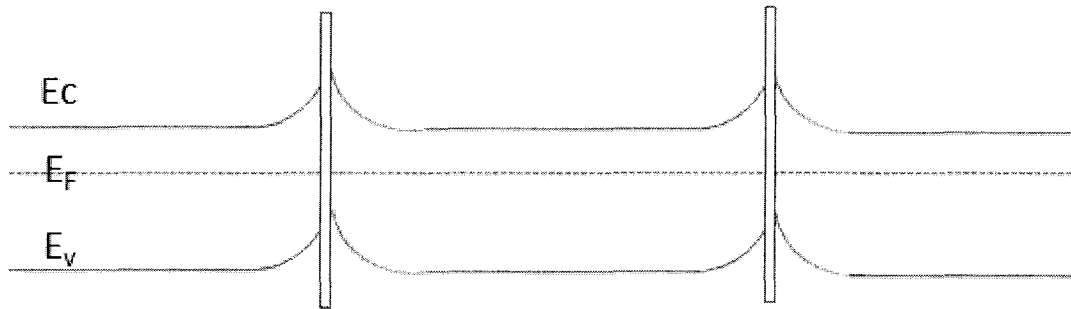


Figure 2.3- Grain boundary barrier and parabolic barriers in polysilicon [40]

When polycrystalline semiconductor is lightly doped, the main blocking factor is the parabolic potential; however a highly doped polycrystalline semiconductor is mainly blocked by grain boundaries.

From the above discussion we can see that the grain boundaries increase the trapping states in polycrystalline material, and therefore can reduce the life time and mobility of the carriers.

Optical properties of poly and single crystalline semiconductors are somehow different. Single crystalline semiconductors tend to have lower optical absorption. This is because the grain boundaries associated with the polycrystalline semiconductors can absorb lower energy light by having states within the bandgap.

As discussed above, the grain boundaries in polycrystalline material influence electrical properties and therefore it is necessary to reduce these trap densities associated with grain boundaries. This can be done by either reducing the effect of grain boundaries or by completely removing them. However since the grain boundaries increase the optical absorption, removing

them may result in lower optical absorption [41]. Passivation can be done by annealing the polycrystalline semiconductor in hydrogen, since hydrogen diffuses into the grain boundary and reduces its effect on electronic and optical properties.

2.1.2 Amorphous material

The similarity of semiconductor bonds in crystalline and amorphous material of the same semiconductor leads to a similar overall electronic structure. Amorphous and crystalline phases of the same material tend to have comparable band gaps. The disorder of the atomic structure however is the main feature that distinguishes amorphous from crystalline materials [42].

Careful observations of amorphous material show that they have more or less exponential tails rather than perfectly sharp edges [43]. Figure 2.4 shows how the abrupt conduction and valence band are deviated to tails in amorphous materials.

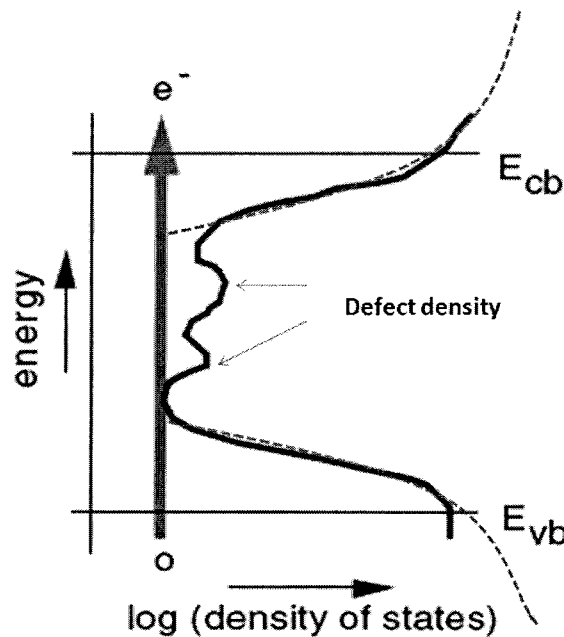


Figure 2.4- Schematic density of states distribution for an amorphous semiconductor showing the band tails and defect states between the conduction and valence bands [43]

The band tails are important properties of amorphous material since electronic transport occurs at the band tails. The reason of having a tail rather than abrupt conduction and valence band originates from the deviations in bond size or bond angle. Band gap states can also be seen in band diagram of amorphous material. These states within the forbidden bandgap usually arise from broken bonds or coordination defects¹. Table 2.1 summarizes the structural disorder that influences the electronic properties.

Structure	Electronic properties
Bonding disorder (e.g. deviations in bond size and angle)	Band tails, localization, scattering
Structural defects (e.g. broken bonds)	Electronic states in the band-gap
Alternative bonding configurations	Electronically induced metastable states

Table 2.1 - Features of atomic structure and the resulting electronic properties [42]

Metastable states are achieved by alternative bonding configurations; for example inducing H₂ into the deposited film.

2.1.2.1 Transport in amorphous material

One of the important properties of amorphous material is their conductivity. Conductivity is a macroscopic quantity that is an average property of carriers moving from site to site. There are three main conduction mechanisms in amorphous materials:

1- Extended state² conduction: Extended state conduction is thermal activation of carriers from E_F to above the mobility edge.

2- Band tail conduction: Tunnelling transitions between localized states at elevated temperatures

(Normally there is no conduction in localized states at zero temperature).

¹ Effect of having different number of bonds for atoms are called coordination effects

² States in conduction edge (mobility edge) in amorphous materials

3- Hopping conduction at Fermi energy: Conduction at the Fermi energy occurs when the density of states is large enough for significant tunnelling of electrons. This conduction is rather weak and tends to dominate in low temperatures.

Illustration of these mechanisms is shown in Figure 2.5.

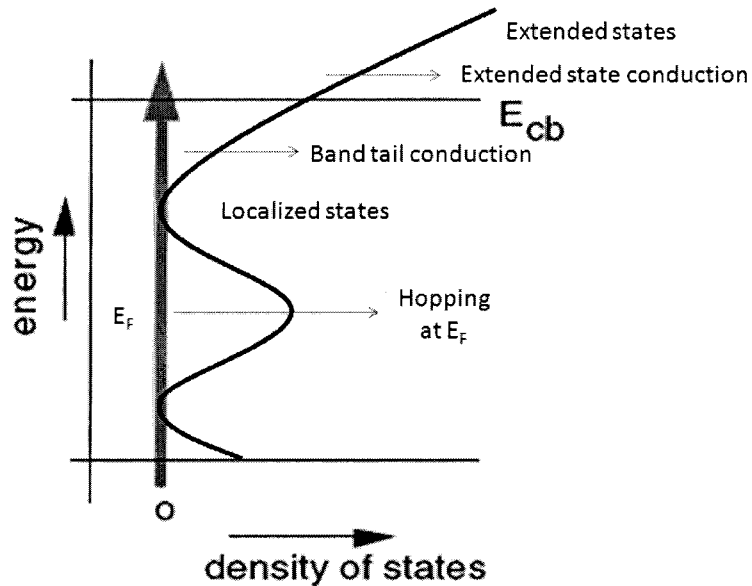


Figure 2.5-Illustration of three main conduction mechanisms in amorphous material [44]

One of the basic studies of amorphous materials is the distinction between localized and extended states and most of the experimental measurements of localized state distribution are based on this property. At zero temperature, carriers in extended states are conducting, but in localized states are not conducting [42]. Basic information on the carrier transport in a-Si:H is obtained from the temperature dependence of the conductivity, but more insight into the transport properties and the effect of localized states comes from work on time-resolved photoconductance [44]. Figure 2.6 shows the linear and log scale time versus photoconductance of a-Si:H at 210K. One can see from this figure that the photocurrent shows decay behaviour. To interpret this, thermalization of carriers needs to be described. An excited electron or hole first

loses energy by many transitions within the band, in which the energy loss is small but frequent in each of these transitions. This process is referred to as thermalization. The thermalization rate decreases as the electron moves into the localized band tail states.

In Figure 2.6 (a), after thermalization of the hot, excited carriers, the photo-generated electrons occupy localized states, with only a few carriers being in extended states. Although in this situation the electron energy is much higher than in thermal equilibrium, further thermalization is slowed down due to the long thermalization time for localized states [44].

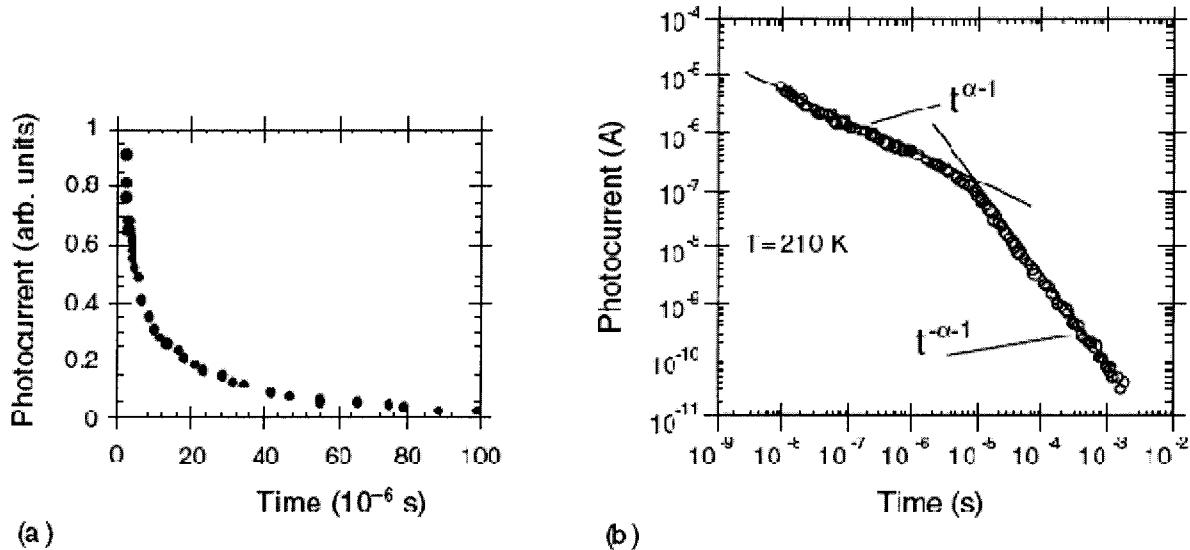


Figure 2.6 -Time resolved photoconductance of a-Si:H (a) Linear scale (b) Log-log sale [44]

Figure 2.6 (b), shows that the decay is following two laws of $t^{\alpha-1}$ and $t^{-\alpha-1}$ where α is called the dispersion parameter. In the initial stage the total carrier density remains constant since recombination and extraction occur at later stages. When the electrons are extracted from the film, the total amount of carriers decrease and the decay turns into $t^{-\alpha-1}$ [44]. In other words, the power law transient photo-response seen by amorphous material is due to a process called

multiple trapping (MT) that current monitors the shallow high mobility states, while the decay of current is due to trapping of carriers in deeper states in the band tails [43].

2.1.2.2 Hydrogenation effects

The concept of hydrogenation of amorphous semiconductors was first established by Harvard group¹, preparing rf diode sputtered semiconductors in 1974 [45]. They sputtered Ge in an argon-hydrogen atmosphere to make a-Ge:H films and investigated the effect of hydrogenation in a-Ge films. Their following works showed that hydrogenation decreases dark current and increases photocurrent because of saturating dangling bonds associated with amorphous sputtered Ge films.

Hydrogen, with its single electron and its small covalent radius, can be used to compensate individual dangling bonds on the void surface of amorphous Ge, and the variation of the electronic properties with hydrogen coverage can be determined. Thus, density of electronic states of fully bonded but hydrogenated amorphous Ge, which near the gap will resemble that of fully coordinated material, can in principal be established [46]. Annealing or using high temperature deposition are other traditional approaches for minimizing the number of dangling bonds but these approaches in addition to changing the void structure of Ge may change network structure and also it is not easy to determine if all the dangling bonds are removed above a certain temperature. Therefore hydrogenation has numerous advantages over the traditional approaches. However H₂ can break or remove weak semiconductor bonds particularly during thin film growth.

¹ A group at Harvard Univ., Cambridge, MA, USA.

2.2 Contact metal

Different metals have different work functions due to their crystal orientation and material characteristics. According to Schottky-Mott theory, the barrier height between the metal and semiconductor is sensitive to metal work functions. However there is little support from the experimental results of metal work function having a great effect on barrier height. Schottky barrier heights are usually determined by the semiconductor and have rather a weak dependence on metal. Mayburg G. *et al.* [47] have determined Schottky barrier height of thirty six metals on n-GaAs. They found no linear relationship between the metal work function and Schottky barrier height as is suggested by Schottky-Mott theory. They found that the linear relationship between metal and semiconductor does not apply to all metal categories, rather to the metals with higher melting points. The influence of metal work functions of Mg, In, Al, and Pd on properties of metal/a-SiC:H Schottky diode is investigated [48]. Their results show that Pd and Al have low leakage currents compared to Mg and In. C. K Tan *et al.* [49] have also shown linear dependence of metal/p-GaN Schottky barrier height on the metal work function. The investigated metals are Zr, Ti, Cr, and Pt.

Chapter3

Theoretical concepts of MSM photodetectors

3.1 Metal-Semiconductor junction

The metal-semiconductor junction is a key structure required for the operation of any semiconductor device, since electrical contact to external components is essential. While the Ohmic contact is most commonly used, a rectifying or Schottky contact has interesting properties making it useful for photodetection.

A metal-semiconductor Schottky junction is developed to have faster response compared to p-n or p-i-n junctions, since in a p-n junction the switching speed is controlled by recombination of minority injected carriers and is of the order of a few microseconds, while in the Schottky diode, it is controlled by the thermalization of hot injected electrons across the barrier and the speed is of the order of a few picoseconds. Furthermore, Schottky diode's simple fabrication makes it a good candidate for many applications. When a specific metal is deposited on a specific semiconductor, a metal-semiconductor junction is formed but it might be either an Ohmic contact or a Schottky contact. These two categories are discussed in the following sections.

3.1.1 Schottky contact

The Schottky contact is of interest for use in electronics mainly due to faster responses compared to the p-n diodes. By faster response it is meant that the switching from conducting mode to non-conducting mode is faster. This rectifying contact is formed by attaching a metal conductor to a lightly doped semiconductor, which is a basis of a Schottky diode [50].

Analysis of an ideal Schottky diode can start with an energy band diagram. The energy band diagram of metal and semiconductor before contact is shown in Figure 3.1 for an n-type semiconductor.

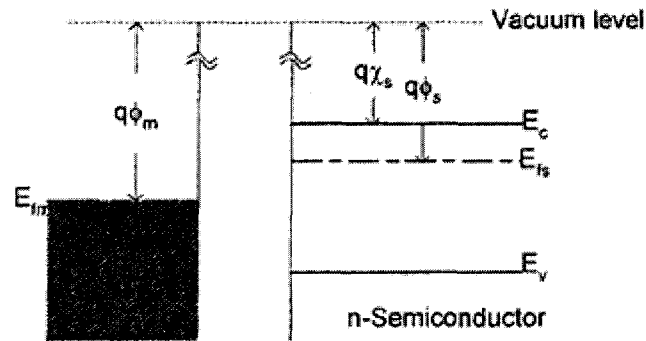


Figure 3.1-Energy band diagram before contact [41]

To explain this diagram a few parameters need to be described:

Vacuum level: Vacuum level energy is the energy of an electron outside solid.

Work function (Φ): Amount of energy required to take an electron from Fermi level to outside of solid.

Electron affinity (χ): Required energy to move an electron from bottom conduction band to outside of the semiconductor.

Consider the situation in which work function of metal is higher than that of semiconductor. When metal and semiconductor are brought together, it will be a system with a unique Fermi level in thermal equilibrium. Fermi level pinning is caused by redistribution of charges throughout system thermal equilibrium which forms the barrier. Figure 3.2 shows the system in thermal equilibrium.

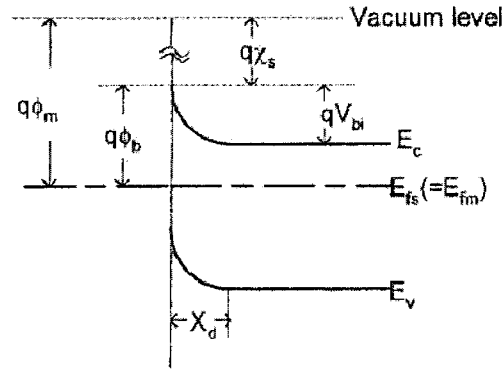


Figure 3.2- Energy band diagram after contact [41].

To have an equilibrium state horizontal line Fermi level, the material with higher Fermi level should contribute electrons to the material with lower Fermi level. Therefore in this case ($\Phi_m > \Phi_s$) electrons flow from conduction band of semiconductor to the metal and they create a depletion region.

There are a few parameters in Figure 3.2 that needs to be defined:

$$\text{Barrier height} = q\phi_b = q(\phi_m - \chi_s) \quad (3.1)$$

$$\text{Built in potential barrier} = V_{bi} = V_D = \phi_b - \frac{1}{q}(E_F - E_C) \quad (3.2)$$

Where q is electron charge, E_F is Fermi level, and E_C is conduction band energy state.

Forward bias condition: If a positive voltage is applied to metal with respect to semiconductor, the metal to semiconductor potential barrier height decreases and this will allow more easy flow of electrons into the metal.

Reverse bias condition: If a negative voltage is applied to metal with respect to semiconductor, the metal to semiconductor potential barrier height increases and electrons will need more potential in order to flow over the barrier height.

It should be noted that in an ideal case, the barrier height from metal to semiconductor does not change as the bias voltage changes, and this is the barrier height for electrons moving from semiconductor to metal that changes by applying different bias voltages.

The energy band diagrams of forward and reverse bias conditions are shown in Figure 3.3.

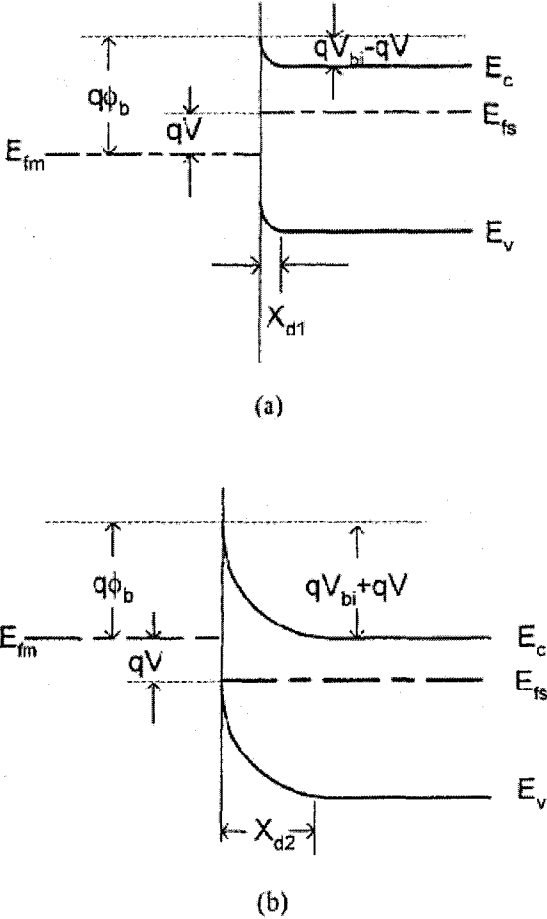


Figure 3.3 - Ideal energy band diagrams of (a) Forward (b) Reverse bias [41]

These diagrams clearly show the barrier height modification with applied bias voltage. In the next section, current transport process through the barrier will be discussed.

3.1.2 Current transport process

Current transport in Metal-semiconductor contacts is due mainly to majority carriers as opposed to a p-n junction where the minority carriers are the main carriers. There are four current processes in a Metal-Semiconductor contact when forward biased [51]:

- 1- Transport of electrons from semiconductor to metal, which is the main current transport in a Metal-Semiconductor contact.
- 2- Quantum-mechanical tunnelling of electrons through the barrier (important for heavily doped semiconductors and the main current transport in Ohmic contacts).
- 3- Recombination in the space-charge region.
- 4- Hole injection from the metal to the semiconductor (equivalent to the recombination in the neutral region).

In addition to the above main current transport mechanisms, there may be edge leakage currents due to high electric field at the contact periphery or at the interface, due to traps at the interface[51].

To describe the current transport of electrons over the potential barrier, Thermionic Emission Theory and Diffusion Theory are derived which describe transport of electrons over the potential barrier. Thermionic Emission Theory is applicable to high-mobility semiconductors while Diffusion Theory is applicable to low-mobility semiconductors. Current density expression of both of the theories are similar, however, the saturation current density is different. Saturation current density for diffusion theory varies more rapidly with the voltage but is less sensitive to temperature compared with the saturation current density of thermionic emission theory.

Thermionic Emission-Diffusion Theory is a synthesis of both of the above theories that is derived from the boundary condition of a thermionic recombination velocity near the metal-semiconductor interface. Therefore an expression for current transport of Thermionic Emission-Diffusion Theory better describes current transportation compared with the above two distinct theories.

The current transport expression for Thermionic-Emission Theory taking into account the tunnelling current is:

$$I = I_o(e^{qV/nkT} - 1) \quad (3.3)$$

Where n is the ideality factor and is equal to 1 in an ideal case, V is the applied bias voltage, k is Boltzmann constant and is equal to 1.38×10^{-23} J/K, and q is the electron charge.

I_o is the saturation current density and is equal to:

$$I_o = A^{**}T^2 e^{(-\frac{q\phi_B}{kT})} \quad (3.4)$$

As can be seen the saturation current depends on the size of barrier height for electron injection from the metal into semiconductor, and is unaffected by the bias voltage. A^{**} is the effective Richardson constant, T is the temperature, and ϕ_{Bn} is the metal to semiconductor barrier height.

This expression is under forward bias condition. When V is positive and greater than a few kT/q , the exponential term is much greater than unity. The current thus increases with forward bias voltage. When V is negative (reverse bias), the exponential term approaches zero and the current density is $-I_o$ [3].

Ideally the reverse current density $-I_o$ should be constant, however, when the M-S contact is biased by a voltage V , there is an external field applied to the contact. Although this field is not

constant with distance, the value at the surface can be used as a good approximation. This external field lowers the work function of a metal by $q\Delta\phi$ which is called image-force lowering. The reduction of the surface work function of metal makes it easy for an electron in the metal to overcome the barrier and move to the semiconductor side, and thus gives rise to a higher thermionic-emission-diffusion current [41]. Therefore the reverse saturation current density is modified to be:

$$I_o = A^{**}T^2 e^{\left(\frac{-q(-\phi_B + \Delta\phi)}{kT}\right)} \quad (3.5)$$

Where;

$$\Delta\phi = \sqrt{\frac{q\varepsilon}{4\pi\varepsilon_s}} \quad (3.6)$$

ε is the maximum electric field that occurs at $x = 0$ and is equal to $\varepsilon = \sqrt{\frac{2qN_D}{\varepsilon_s} \left(V + V_{bi} - \frac{kT}{q}\right)}$, where N_D is the doping density, V_{bi} is the intrinsic barrier of the diode, and V is the applied voltage.

If the barrier height is sufficiently smaller than the bandgap so that the generation-recombination current is small in comparison with the Schottky emission current, then the reverse current will increase gradually with the reverse bias as given in the equation above. Edge leakage current however is the most dominant current for Schottky diodes. To eliminate this effect, metal-semiconductor diodes can be fabricated using a diffused guard ring [52].

Since the current transport process is closely related to depletion layer, therefore depletion layer characteristics like its width, capacitance, are illustrated in the next following sections.

3.1.3 Depletion layer characteristic

3.1.3.1 Width and electric field

Assuming an abrupt junction, where the charge density in the depletion layer for $0 < x < x_n$ is qN_D , and for $x > x_n$, $N_D = 0$ and also $\epsilon_s = 0$. The expressions for depletion layer width and electric field are as follows:

$$w(\text{depletion width}) = \sqrt{\frac{2\epsilon_s}{qN_D} \left(v_{bi} - v - \frac{kT}{q} \right)} \quad (3.7)$$

Where; the $\frac{kT}{q}$ term arises from the contribution of the majority-carrier distribution tail (electrons in n side).

$$|\epsilon(x)| = \frac{qN_D}{\epsilon_s} (w - x) = \epsilon_m - \frac{qN_D}{\epsilon_s} x \quad (3.8)$$

Where; ϵ_m is the maximum field strength that occurs at $x = 0$ which is presented in the previous section too.

3.1.3.2 Junction capacitance

The space charge Q_{sc} per unit area of the semiconductor and the depletion layer capacitance C per unit are given by the following equations:

$$Q_{sc} = qN_D W = \sqrt{2q\epsilon_s N_D \left(V_{bi} - V - \frac{kT}{q} \right)} \quad \frac{C}{cm^2} \quad (3.9)$$

$$C \equiv \frac{|\partial Q_{sc}|}{\partial V} = \sqrt{\frac{q\epsilon_s N_D}{2(V_{bi} - V - kT/q)}} = \frac{\epsilon_s}{W} \quad \frac{F}{cm^2} \quad (3.10)$$

Equation

(3.10) can be rearranged as:

$$\frac{1}{C^2} = \frac{2(V_{bi} - V - kT/q)}{q\epsilon_s N_D} \quad (3.11)$$

$$-\frac{d(1/C^2)}{dV} = \frac{2}{q\epsilon_s N_D} \quad (3.12)$$

$$N_D = \frac{2}{q\epsilon_s} \left[-\frac{d(1/C^2)}{dV} \right] \quad (3.13)$$

By plotting $1/C^2$ versus V , a straight line should be obtained when having a constant N_D in depletion layer. This method can be used to find doping profile [51].

3.1.4 Ohmic contact

An Ohmic contact follows ohm's law and the current can flow in both of the directions and the junction does not have a rectifying behaviour. An Ohmic contact can be formed by depositing a metal conductor to a heavily doped semiconductor, however if the semiconductor is lightly doped, it becomes a Schottky contact. Ideal metal-semiconductor contacts are Ohmic when the charge induced in the semiconductor in aligning the Fermi levels is provided by majority carriers. For example, in the $\Phi_m < \Phi_s$ (n-type) the Fermi levels are aligned at equilibrium by transferring electrons from the metal to the semiconductor. This raises the semiconductor electron energies (lowers the electrostatic potential) relative to the metal at equilibrium. In this case the barrier to electron flow between the metal and the semiconductor is small and easily overcome by a small voltage. Similarly the case $\Phi_m > \Phi_s$ (p-type) results in easy hole flow across the junction [53].

Contact resistance R_c can be determined for a contact and is an important figure of merit for Ohmic contacts. R_c can be determined by finding derivative of current density (J) with respect to voltage when evaluated at zero bias voltage [51]:

$$R_c = \left(\frac{\partial J}{\partial V} \right)_{V=0}^{-1} \quad (\Omega - cm^2) \quad (3.14)$$

For metal contacts with lower doping concentrations, the thermionic-emission current dominates the current transport, and therefore contact resistance expression will be [51]:

$$R_c = \frac{k}{qA^*T} \exp\left(\frac{q\phi_B - \Delta\phi}{kT}\right) \quad (3.15)$$

Where A^* is the effective Richardson constant for thermionic emission theory neglecting the effects of optical phonon scattering and quantum mechanical reflection. For contacts with higher doping, the tunnelling effect dominates and contact resistance is derived to be [51]:

$$R_c = \exp\left(\frac{2\sqrt{\epsilon_s m^*}}{\hbar} \left(\frac{\phi_{Bn}}{\sqrt{N_D}}\right)\right) \quad (3.16)$$

Where $\phi_{Bn} = q\phi_B - \Delta\phi$

Where m^* is the effective mass of semiconductor, and \hbar is plank's constant. This equation shows that in the tunnelling range the specific contact resistance depends strongly on doping concentration.

3.2 MSM theory

MSM photodiodes are mostly in the form of interdigitated electrodes on top of active layer.

Figure bellow shows the MSM configuration from top and cross section views.

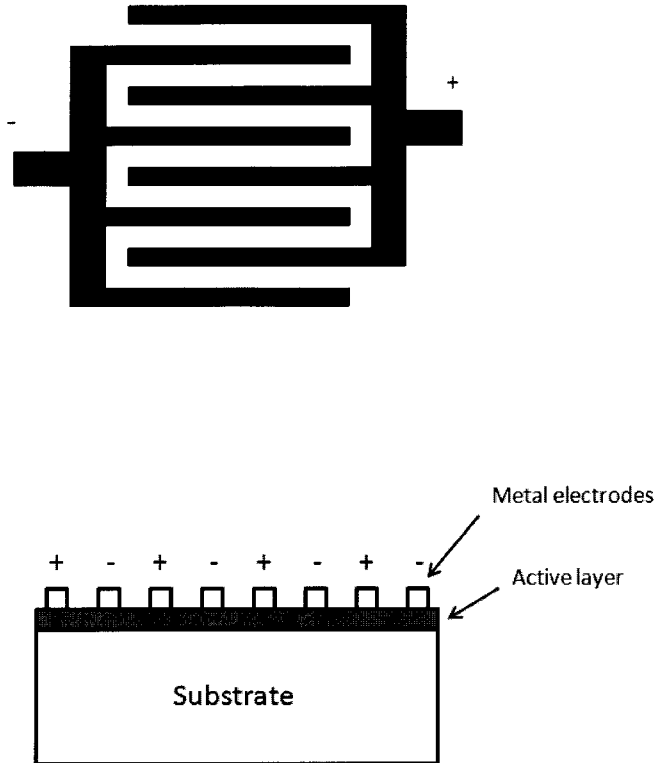


Figure 3.4- Top and cross section view of MSM interdigitated photodiodes

Light absorption occurs in the area between the electrodes which is the active layer of the photodetector. Full description of the theoretical behaviour of the MSM structure is treated by Sze [54].

3.2.1 Dark current

According to Sze [54] , an MSM detector consists of two back to back Schottky diodes. Figure bellow shows the energy band diagram of the MSM detector at thermal equilibrium where ϕ_{n1} and ϕ_{n2} are barrier heights of the two schottky contacts, V_{D1} and V_{D2} are the built in potentials respectively, and L is the spacing between electrodes. A symmetrical MSM structure forms when $\phi_{n1} = \phi_{n2}$, and the area of electrodes is equal.

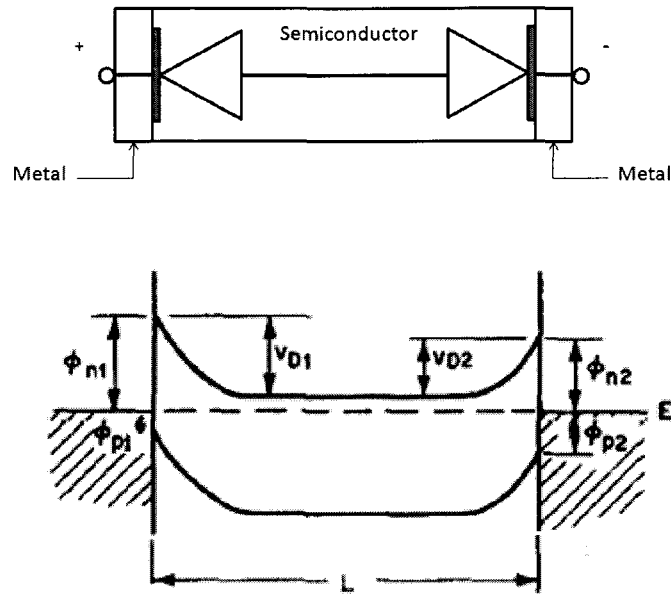
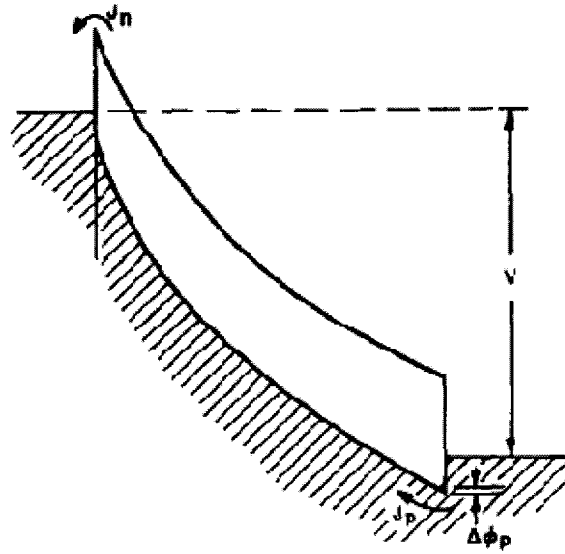


Figure 3.5- (a) Schematic diagram (b) Energy band diagram of MSM structure [54]

When a negative bias is applied to contact 1 with respect to contact 2, contact 1 is reverse biased and contact 2 is forward biased. The applied voltage is shared between the two contacts: $v = v_1 + v_2$, where v_1 and v_2 represent the voltage drop across the contacts. Since contact 2 is reverse biased, its depletion region is wider than contact 1, and most of the voltage drop will be across contact 2. This is shown in Figure 3.6. As the bias voltage increases, depletion width of the contacts increases. V_{RT} , which is called reach-through voltage is a point that the depletion widths of the contacts reach to each other and therefore $w_1 + w_2 = L$. Further increase of the voltage to a point that $w_2 = 0$ and electric field of contact 2 is zero, is the condition that is called flat-band voltage (V_{FB}). Applying higher voltages is limited by avalanche break down of the MSM structure. Figure 3.7 better illustrates all the above conditions.



(c)

Figure 3.7-(a) Condition of reach-through voltage (b) Flat band condition (c) $V > V_{FB}$ [54]

Dark current characteristic of an MSM structure can be different depending on ϕ_{n1} and ϕ_{p2} . Therefore the material of the activation layer and metal, deposition process, and structure of the device can make different characteristics of the MSM diode.

Two cases of I-V characteristics where; $J_{n1} \gg J_{p2}$ and $J_{n1} \ll J_{p2}$ are discussed and other I-V characteristic may fall between these two cases depending on their barrier heights for electrons and holes.

In a simple Metal-Semiconductor contact, there is only one type of carrier that corresponds to dark current of the contact. However in MSM structure thermionic emission of both electrons and holes contribute to dark current characteristic of the detector. Assuming the first case where $J_{n1} \ll J_{p2}$, under an applied bias voltage, one of the diodes is forward biased and the other one is reverse biased. If a low negative voltage is applied to contact No. 1 with respect to contact No. 2 (contact 1 reversed biased, and contact 2 forward biased), the thermionic emission current is due

to transfer of electrons from contact 1 to contact 2. There is also thermionic emission of holes from contact 2 to 1 but in case of $J_{n1} \ll J_{p2}$ this current is small at low voltages. When the voltage reached reach-through voltage, the depletion layers of the contacts reach to each other, and this is the point that thermionic emission of holes from contact 2 starts to increase and total current starts to increase quickly after reaching V_{RT} . Further increase of the voltage to V_{FB} , will reduce the rate of increasing current due to barrier lowering effect. Eventually the avalanche break down will occur and the schottky contact will fail.

Now if $J_{n1} \gg J_{p2}$ (ϕ_{p2} is high) the hole current will always be smaller than electron current, so that the total current is almost equal to electron current and contact 2 will act like an Ohmic contact with no injection. As the voltage increases, eventually the break down will occur at which the current will rapidly increase. Figure 3.8 shows current versus bias voltage of both of the cases [54].

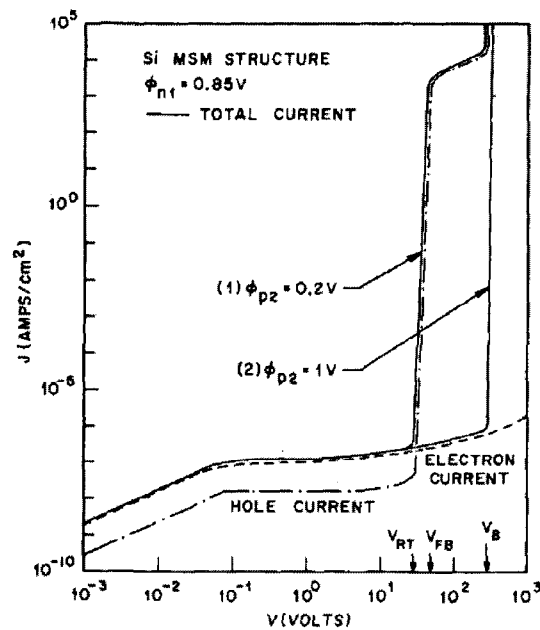


Figure 3.8-Theoretical I-V characteristics for a Si symmetric MSM with $N_D = 4 \times 10^{16} \text{ cm}^{-3}$ and $L = 12 \mu\text{m}$ at 300°K where Case (1) : $\phi_{n1} = 0.85V$ and $\phi_{p2} = 0.2V$; Case (2) : $\phi_{n1} = 0.85V$ and $\phi_{p2} = 1V$ [54]

Figure 3.8 has a log-log scale in order to show a broader range of voltage response.

MSM detectors with low dark current are most desirable detectors for optical communication systems because a higher dark current would cause difficulty in light signal detection. To decrease the dark current there is a trade-off between the electron injection at reverse-bias contact and hole injection at forward bias contact. At low bias voltages the main source of dark current is from electron transportation and in higher voltages hole current is the main source of current transportation. Therefore for dark current reduction, both electron and hole current should be decreased. The lowest dark current is achieved when $q\phi_n = q\phi_p = Eg/2$. This is normally the rule to choose the appropriate electrode metal for MSM detector [41].

3.2.2 Barrier height / Saturation current / Quality factor

Barrier height can be found from the following equation [55]:

$$\phi = \frac{kT}{q} \ln \left(\frac{A^{**}ST^2}{I_o} \right) \quad (3.17)$$

Where I_o is the saturation current and is equal to:

$$I_o = A^{**}ST^2 \exp(-q\phi/kT) \quad (3.18)$$

k is Boltzman's constant, T is the absolute temperature in Kelvin, q is the electronic charge, $A^{**}A$ is the Richardson constant, and S is the contact area.

Therefore to find barrier height of an MSM detector saturation current should be found. As mentioned before, equation bellow is the conventional equation for thermionic emission of carriers in MSM detectors[55]:

$$I = I_o \exp(qV/nkT) \cdot (1 - \exp(-qV/kT)) \quad (3.19)$$

Where n is the quality factor of the MSM photodiode.

Note that this equation includes the effect of barrier height lowering due to electric field, tunneling effects, and carrier recombination in the space-charge region of Metal-semiconductor contact, by adding $\exp(qV/kT)$ to the more conventional equation of: $I = I_o \cdot (1 - \exp(-qV/nkT))$. The difference between these two equations vanishes when $v > 3kT/q$ [55].

The above equation can be rearranged as follows:

$$\frac{I \exp(qV/kT)}{(\exp(qV/kT) - 1)} = I_o \exp(qV/nkT) \quad (3.20)$$

That shows that the plot of $\ln\left(\frac{I \exp(qV/kT)}{(\exp(qV/kT) - 1)}\right)$ versus V is just linear and the slope of the line is equal to q/nkT , from where the quality factor of the Schottky diode can be calculated. Furthermore, intercept point of the linear line at V=0 axis gives out saturation current.

3.2.3 Responsivity

Responsivity is a figure of merit for detectors that describes how efficiently the light is converted into current which is defined as:

$$\mathfrak{R} = \frac{I_{ph}}{P_o} (A/w) \quad (3.21)$$

I_{ph} is the photocurrent and P_o is the incident power on the sensor area. Responsivity is very easy to measure and many have stated the performance of their device in A/w and therefore it is a good criteria in a sense that it is easy to compare the results with other works. However it does not include dark current effects and it might not be the best case for showing the performance of

the photodiode and therefore along with responsivity, many indicate the dark current of photodiode.

Quantum efficiency is another figure to show the performance of a photodiode and is defined as the ratio of the number of electrons generated by the detector to the number of photons incident on the detector.

$$\eta_e = \eta_i(1 - R) \frac{1}{\Gamma} = \eta_i(1 - R) \frac{s}{s + w} \quad (3.22)$$

R is the reflectivity at the air-semiconductor interface and reducing R enhances the performance of photodiode. η_i is the internal quantum efficiency and is equal to $\eta_i = (1 - e^{-\alpha d})$, describing the collected photocurrent to the number of photons in the active layer, which depends on absorption coefficient α , and the length of the absorbing layer d.

For the geometry shown in Figure 3.4, the detector is generally illuminated from the top surface. In this configuration, the metal electrodes block a fraction of the light from entering the semiconductor and thus reduce the maximum achievable external quantum efficiency by a factor associated with the “fill factor” of the electrodes, given by:

$$\Gamma = \frac{w}{s + w} \quad (3.23)$$

Where s is the spacing between adjacent electrodes and w is the width of the electrodes.

Quantum efficiency however is not easy to calculate and therefore making it not the best figure of merit for photodiodes.

Since the quantum efficiency η_e compares the incident photon flux to the collected photocurrent, it can be defined as:

$$\eta_e = \frac{I_{ph}/q}{P_o/h\nu} \quad (3.24)$$

Where ν is the frequency of the incident light.

3.2.4 Capacitance

As outlined, one of the advantages of the interdigitated MSM is its low capacitance per unit area. Typical photolithographically defined devices have electrode fingers widths of $\sim 1 \mu\text{m}$ and interdigital spacings of $1\text{-}3\mu\text{m}$ [56]. In the Carleton University microfabrication laboratory the smallest practical size using in-house mask making is $2.5\mu\text{m}$.

A theoretical model based on conformal mapping technique demonstrated that the capacitance of an interdigitated electrode can be determined as [57]:

$$C = 0.226NL\epsilon_o(\epsilon_s + 1)(6.5\eta^2 + 1.08\eta + 2.37) \quad (3.25)$$

Where $N = L/2(t + D)$ is number of finger pairs and $\eta = D/(t + D)$ is finger to period ratio. D is finger width and t is the spacing. This equation shows that reducing the aperture of the PD and number of interdigitated contact pairs could reduce the capacitance of the device. The figure below shows the capacitance of interdigitated electrodes with different gap size [56].

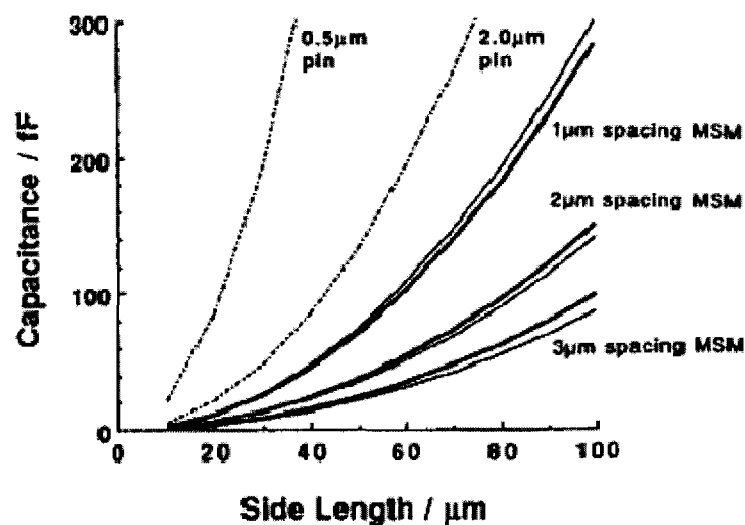


Figure 3.9-Capacitance versus side length of MSM and pin Photodetectors [56]

Generally, increasing the gap between diode fingers decreases the capacitance; however transit time of carriers and detector response increases.

Capacitance of the junctions changes with the bias voltage applied. In the next section, capacitance will be described as a function of bias voltage.

3.2.4.1 Capacitance vs. Bias voltage

Having two contacts, leads to having two capacitances in series due to each contact for $V < V_{RT}$.

Therefore total capacitance would be [52]:

$$C = \frac{C_1 C_2}{C_1 + C_2} \quad (3.26)$$

Where

$$C_1 \equiv \sqrt{\frac{q \epsilon_s N_D}{2(V_1 + V_{D1})}} \quad (3.27)$$

$$C_2 \equiv \sqrt{\frac{q \epsilon_s N_D}{2(V_{D2} - V_2)}} \quad (3.28)$$

By increasing the voltage most of the voltage drop will be across contact 1 and the capacitance

is: $\cong \sqrt{\left(\frac{q \epsilon_s N_D}{2}\right) \left[\frac{1}{\sqrt{(V+V_D)+\sqrt{V_D}}}\right]}$. From this equation, the capacitance has a maximum point, and

by increasing the voltage the zero-bias capacitance increases until it reaches its maximum and then starts to decrease with higher voltages applied.

For $V > V_{RT}$, semiconductor is completely depleted and the capacitance per unit area is equal to

$$C = \epsilon_g / L .$$

Figure 3.10 shows capacitance versus bias voltage applied to MSM-PD [52].

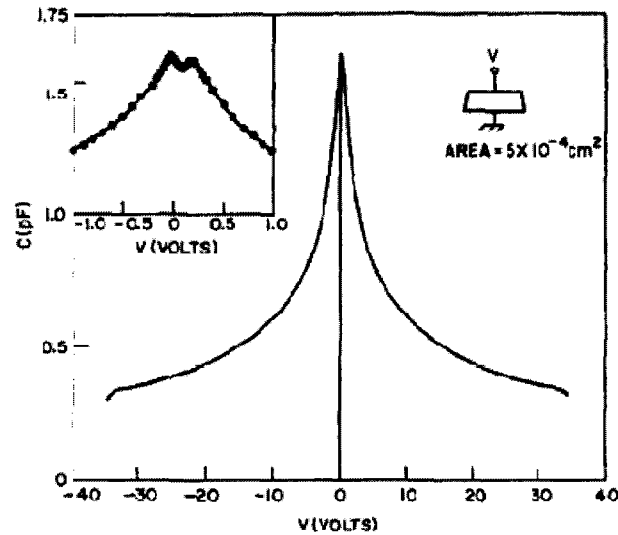


Figure 3.10- Capacitance voltage characteristics of MSM detector [54]

3.2.5 Detectivity

A “figure-of-merit” for infrared detectors is D^* (deestar), whereby detectors of differing area can be compared. It is related to the noise equivalent power (NEP) in watts, the lowest power a detector can detect at a signal-to-noise ratio of 1 as

$$D^*(l, f, B) = (AB)^{1/2}/NEP \quad (3.29)$$

Where; A is the detector area. The optical bandwidth B (often taken to be 1 Hz), frequency of signal modulation (f), and operating wavelength (l) must be stated [2].

Detectivity is a good figure to show the overall performance of the photodiode, but not many of the papers state the performance in detectivity making it hard for comparing the results with other works.

Generally many works tend to show the performance of the photodetectors by the responsivity value and saturation current of the device as already mentioned. However some works report the performance of their device in detectivity or more commonly quantum efficiency in order to show a broader range of device characteristics in one value. Here in this work the results are presented by responsivity value.

Chapter4

Material investigation, fabrication, and characterization

4.1 Choice of sputter deposition

Sputter deposition is a physical vapour deposition technique that the films are deposited atomically by means of ionic species. There are several sputtering systems for the purpose of thin-film deposition. Among these sputtering systems, the basic model is the dc diode sputtering system, and the other systems are improvements on the dc diode sputtering system. The dc diode sputtering system is composed of a pair of planar electrodes that one of the electrodes is a cold cathode and the other is an anode. Target material is on the top surface, and the substrate is placed on the anode. After the plasma is formed (usually with a spark), Ionized gas atoms strike the cathode and cause emission of atoms from the target material. The emitted atoms collide with the gas molecules and eventually condense on the substrate [58].

RF Magnetron sputtering system is another system for sputtering that is used to deposit Ge thin films in this project because of the availability in Carleton university microfabrication laboratory. Figure 4.1 shows a typical RF sputtering system. In RF sputtering systems, the DC power is replaced by an RF power and the metal target is replaced by an insulator. Magnetron sputtering systems have the plasma to be formed with presence of a magnetic field.

The main reason of focusing on sputter deposition in this project is that it is a low temperature deposition technique, with lower cost, suitable for integration with optical MEMS applications that was the initial motivation of this thesis project. However, the film qualities are usually lower comparing with deposition techniques like UHV-CVD that are more expensive.

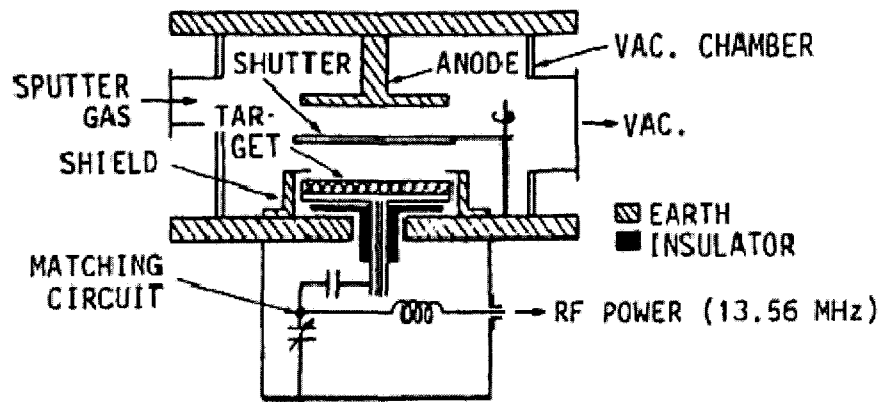


Figure 4.1 – Example of an RF sputtering system [58]

Although germanium has been deposited by vacuum evaporation and sputtering techniques, the films usually show p-type conductivity, even though the source materials were heavily doped with n-type impurities. Some authors attributed this result to impurities, while others considered it to be due to imperfection in the crystalline structure of the films and surface states [59], bulk properties of Ge [60], or in the case of silicon, contamination of the structural defects [61].

Crystalline Ge deposited thin films are of interest because of their lower defects and therefore lower leakage current. Some works have investigated the effect of deposition temperature of crystalline structure of Ge films that will be discussed in detail in the next section. Furthermore, film thickness and hydrogenated amorphous films are studied in this project. Next section is a review on the sputtered Ge films that were the starting point of this project, and the characterization of the films is followed by the next section.

4.2 Review of sputtered Ge thin films

K. B. Sundarm *et al.* [62] have looked at RF sputtered Ge thin films at different deposition powers. This paper has reported a technique to produce both n and p type doping with different

concentrations between $10^{15} - 10^{18}$ carrier/cm³. They basically change the input power level and get different doping concentrations. Furthermore, they show how the sheet resistivity and carrier mobility changes by changing input power level. The following table shows the deposition conditions of their experiment for a glass substrate:

Vacuum pressure	Ar pressure	RF frequency	Input power	Deposition duration	Temperature	Ge source
3×10^{-6} Torr	2-3mTorr	13.65 MHz	25 to 100 w	1 to 2 Hr	500°C	Bismuth (n-type)

Table 4.1- Deposition conditions of samples prepared in [62]

They found that at higher sputtering powers, the films show p-type conductivity, and as the power level is reduced, resistivity increases. At around 40W the films have highest resistivity, and further decreasing the power, the films show n-type conductivity and sudden decrease in resistivity.

They state that the general p-type conductivity observed in the films is attributed to the crystalline defects, and by decreasing the power level, deposition growth rate decreases hence crystalline defects reduces and lower p-type carriers will be observed.

In addition, they changed the pressure of Ar gas to see how the range of conversion from p to n type changes. According to their results, as the pressure increases the conversion from n to p occurs at higher deposition rates increases. Table bellow is the summary of their work:

Ar gas pressure	p to n type conversion power level
2m Torr	40-50W
2.5 mTorr	50-60W
3 mTorr	Always n-type (up to 100W)

Table 4.2- Ar pressure vs. p to n conversion power [62]

In this project, Ge thin films were deposited at different RF power levels in order see if the same characteristics are achieved.

Y. Yang et al. [63] have characterized crystal structure of magnetron sputter deposited thin films by X-ray and Raman spectroscopy. They have shown that the films grown at temperatures bellow 350°C and above 450°C are amorphous. Their Xray results show that the best growth temperature for Ge deposition is 400°C. Here in this project, crystal structure of the films has been characterized with Xray diffraction at two different temperatures of 250°C and 450°C and the results are presented in the following section.

Electrical properties (carrier concentration and mobility) of sputtered Ge films with different film thickness was investigated and measured in different temperatures in [64]. Their results show that carrier concentration rapidly decreased with distance from the interface and became approximately constant beyond a film thickness of about 3 μm . In this project, the samples have thickness of about 2 μm to have a reasonable carrier concentration and mobility.

Hydrogenated amorphous films were also looked at in this project. Min H., has characterized sputtered Ge at different Hydrogen concentrations with ESR¹ experiment [65]. ESR is one of the few experiments that give information on the structure of defects. g-value is a term in this experiment that is utilized to find out how the local configuration of defects changes. A free electron has a g-value of 2.0023 and when it is surrounded with other materials, this value shifts because of spin-orbit coupling to the other electron states [42]. The g-shift contains detailed information about the local bonding structure of the defects. Defect states near the valence band tend to have the largest g-shifts because the coupling to valence band is greater than to

¹ Electron Spin Resonance

conduction band. In Min H. work [65], they have determined the relation between hydrogen concentration and g-value. According to their results, as the hydrogen concentration increases, g-value decreases which show changing of dangling bond structure. This could also mean that as the hydrogen concentration increases, the defect states energies are more likely near conduction band and therefore optical response increases. They suggest that decrease of g-value is because H₂ atoms increase the flexibility of the network structure and reduce dangling bonds of the film. The best quality of a-Ge:H films with respect to Urbach energy¹ have also been obtained at low argon pressure and low dc power at 147°C substrate temperature [66]. Based on this results Ge films with different hydrogen concentration in plasma gas were sputtered and characterized with resistivity measurements and optical response (resistivity measurement is done only on a 5%H₂ concentration in order to compare hydrogenated and non-hydrogenated film resistivities, and higher H₂ concentrations will be characterized based on optical response in chapter5).

4.3 System parameters and characterization of sputter deposited Ge films

Samples with different RF power, temperature, and hydrogen concentration were sputter deposited in Varian sputtering system at microfabrication laboratory of Carleton University, referring to the above works. System parameters are all summarized in Table 4.3. In all the cases the Ar pressure in the vacuum is about 4mT.

¹ One of the standard measures of electronic disorder in amorphous semiconductors and is determined by drawing a tangent to the absorption spectrum. In other words it is a measure of largest conduction and valence band edge

Sample No.	Sub /Dep. temperature	RF power	Flow rate	Deposition duration	Thickness	Comments
1	Silica/250°C	200w	Ar @24 sccm	16 min	1µm	-
2	Silicon/450°C	200w	Ar @25 sccm	16 min	2µm	-
3	Silicon/450°C	200w	Ar @25 sccm	16 min	2µm	-
5	Silicon/450°C	200w	5%H ₂ Ar @25 sccm	16 min	2µm	-
8	Silicon/450°C	100w	Ar @25 sccm	30 min	2µm	-
9	Silicon/450°C	100w	Ar @25 sccm	30 min	2µm	H ₂ annealed in furnace for 10 mints at 400°C
10	Silicon/450°C	40w	5%H ₂ Ar @25 sccm	80 min	2µm	
11	Silicon/450°C	40w	Ar @25 sccm	80 min	2µm	Rapid Thermal Annealed at 700°C for 10 seconds

Table 4.3- Samples deposited under different system parameters

Silica is a glass and the reason for using silica in the first sample was to more easily identifying Ge, since Silicon and Germanium have similar appearance but are still distinguishable. Sample 2 is deposited on cleaned Si wafer, but all other samples are deposited on gate-oxide Silicon wafers. In the following two sections, the characterization results of the films based on X-Ray diffraction and film resistivity is demonstrated.

4.3.1 X-ray diffraction

Effect of deposition temperature on crystal structure was determined with X-Ray diffraction method on samples 1 and 2 with different deposition temperature. Crystal structure of Ge film was investigated using X-ray measurements in Carleton University at department of chemistry. Figure 4.2 shows the X-ray diffraction spectroscopy of the two samples. The peaks in this figure show some crystalline structures in both of the films that contribute to Ge(111), Ge(400), and the

substrate Si(004). There is however other peaks in the film that might be due to defect network within the film.

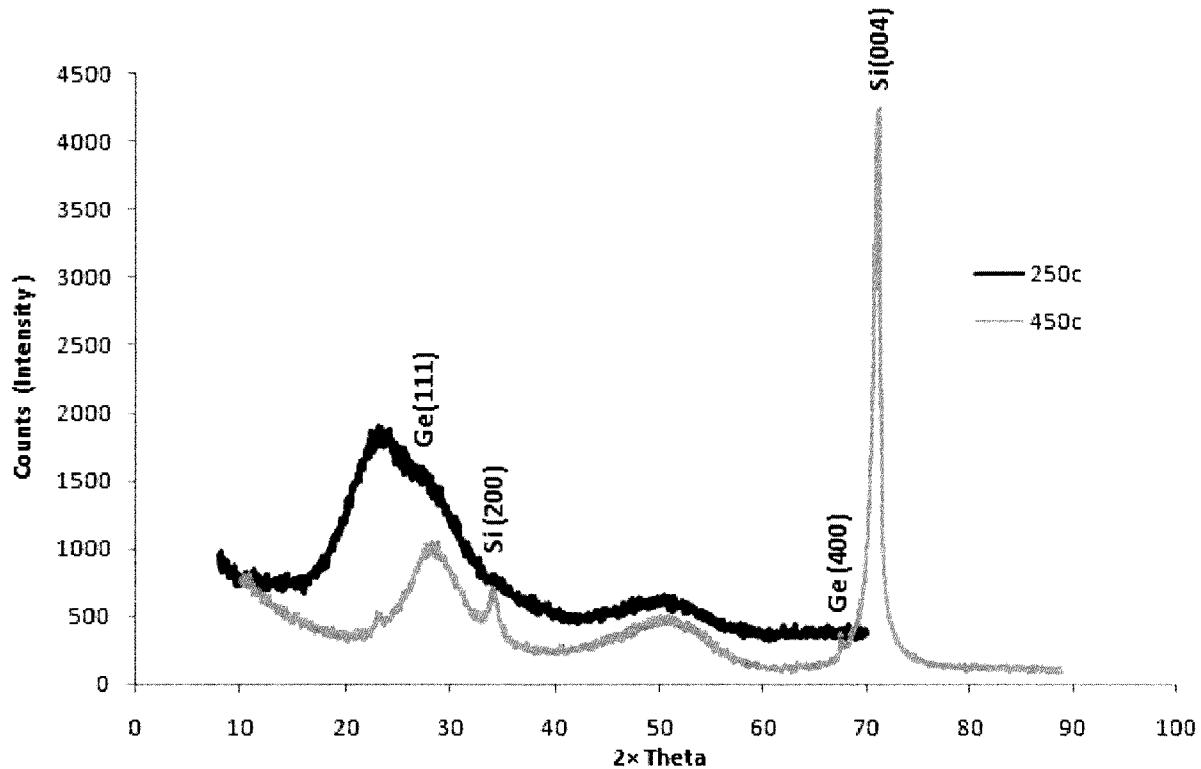


Figure 4.2- Xray diffraction results of sample 1 (250°C) and sample 2 (450°C)

As can be seen, both the 250°C and 450°C samples show some crystalline evidence in the film; however the intensity at these peaks is not so high that these films are considered to be amorphous rather than crystal. Y. Yang et al. [63] found that there is an optimum sputtering deposition temperature for Ge films (400°C). They suggest the reason is that at lower growth temperature, the slowdown of the surface migration makes the deposited atoms frozen thus preventing their crystallization. On the other hand, Ge islanding that occurs at high deposition temperatures make the surface of the Ge corrugated. In this work, since generally at higher temperatures thin films show better overall qualities (closer to bulk), deposition temperature was kept at 450°C.

4.3.2 Resistivity

Effect of different power (200W, 100W, and 40W), hydrogen concentration (0%, and 5%), H₂ annealing, and rapid thermal annealing on resistivity of the film is investigated by 4point probe measurements. Sheet resistivity was calculated with Van der Pauw law ($R_s = 4.532 \left(\frac{\Delta v}{I}\right) \Omega/\text{square}$) using $\frac{\Delta v}{I}$ found from the 4 point probe measurements. Table 4.4 shows all the resistivity results for the samples. A quick description is also included for easier following and complete system parameters can be found in Table 4.3.

Sample number	Quick description	Resistivity Ω/square
3	200W RF	7M
5	200W RF, Hydrogenated	42M
8	100W RF	5M
9	100W RF, H ₂ annealed	5M
10	40W RF, Hydrogenated	1M
11	40W RF, RTA	In k Ω range

Table 4.4-Resistivity of different samples

As can be seen, resistivity of sample 5 is the highest and therefore it shows that existence of hydrogen atoms in the plasma (and therefore its incorporation in Ge films) has a strong effect in properties of the sputtered Ge. Defects in the sputtered film can be a source of dark current. Hydrogen forms H-Ge bond with dangling bonds in sputtered Ge thin film and therefore reduces the amount of defects, leading to higher film resistance.

As can be seen in Table 4.4, even though sample at 40W RF power was deposited in 5% hydrogen (sample 10), it had quite lower resistivity compared to the sample deposited at 200W without hydrogenation (sample 3). Reducing the power based on [62] however did not seem to

decrease the amount of defects and the reason might be that at lower powers the deposition rate decreases and therefore the plasma gas atoms may land on the target and therefore increase the defects in the film. Rapid thermal annealing of Ge at 700°C for 10 seconds was expected to make better crystalline structure of the film, however many parts of the film were corrugated and the film resistivity was so low that it was hard to measure the exact resistivity number. The reason might be that the annealing temperature was high for Ge so that it destroyed the film.

Resistivity results of sample 8 and sample 9, that had same system parameters except sample 9 was hydrogen annealed at 400°C, shows that the annealing did not affect the resistivity of the films base on Table 4.4. The reason might be that the annealing temperature was lower than deposition temperature and it did not make too much difference in the quality of the films.

4.4 Conclusion

In this chapter, films with different system parameters were fabricated and characterized. It was found that deposition temperature of 250°C, and 450°C show some crystalline evidence in the XRD spectra, however they are likely to be amorphous because the intensity of the peaks are not too high and sharp. The samples were deposited with 450°C since generally higher growth temperatures show better crystalline structures.

Moreover, RF power of 200W, and hydrogenation of the films showed higher film resistivity because of better film quality at higher powers and lower defect density of hydrogenated films due to hydrogen incorporation in the films.

Chapter5

MSM photodetector fabrication and characterization

5.1 Fabrication

MSM structures with metal dot electrodes and interdigitated electrodes with different Ge hydrogen concentration and device design were fabricated in this project. After a section on substrate preparation, fabrication of the samples with different metal electrode structures (dots, interdigitated electrodes) is presented along with the all the lithography steps. Characterization is based on dark current and photoresponsivity of the detectors, and these characteristics are summarized in two main tables in each section for all the samples.

5.1.1 Substrate preparation; oxide on Si

Depositing Ge directly on top of Si substrate showed that the current passes through Ge-Si junction, and therefore shows Ge-Si junction characteristics rather than metal-Ge characteristics. That is because resistivity of Ge layer is higher than Si and current tends to avoid passing through Ge. To avoid this, wafers covered with 100nm gate-oxide layer were used acting as an insulator between the Ge active layer and Si substrate. The samples were kept in vacuum before any lithography, however Ge reacts with air and its surface oxidizes. This oxide layer is usually removed by the water used in lithography processing steps.

5.1.2 C-V dots

The MSM photodetectors were first tried using the CV dot shadow masks of the Balzer evaporator in microfabrication laboratory of Carleton University for faster processing. 500nm Al

metal dots of 1.8mm radius were evaporated on all of the samples that are mentioned in previous chapter for characterizing their metal-semiconductor diode. Figure 5.1 shows the picture of dots with the probes on them. In addition, Titanium was evaporated on Ge with same deposition conditions (as sample 3) to see how different metals change device characteristics.



Figure 5.1- Picture of the CV dots with the probes on each dot

Since all the deposited samples were amorphous, a 2 inch single crystalline n-type Ge(100):Sb wafer of .005-.02 Ohms/cm sheet resistivity was also used as active layer in order to compare crystalline and amorphous properties. The wafer was cleaved into a few pieces, and then 500nm Al metal was evaporated on one of the pieces (sample 6), and 200nm Au was evaporated one of the other pieces (sample 7) to verify device junction characteristics of crystalline Ge. Sample descriptions are all summarized in Table 5.1.

5.1.3 Interdigitated MSM structures

The main aim of this project was to fabricate MSM interdigitated electrodes and the dots were used for faster processing in the beginning of the project. This section illustrates different MSM structures and their fabrication process.

5.1.3.1 Metal on semiconductor

The first MSM structure was electrodes with $2.5\mu\text{m}$ width and spacing and area of $100\times 100\mu\text{m}^2$ attached to probe pads of 50 by $50\mu\text{m}$ with 19 interdigitated electrodes patterned on Ge active layer. The mask was already designed by R. Macdonald [67] and was also used by J. Liu in [41]. Figure 5.2 shows the fabricated top view of the device.

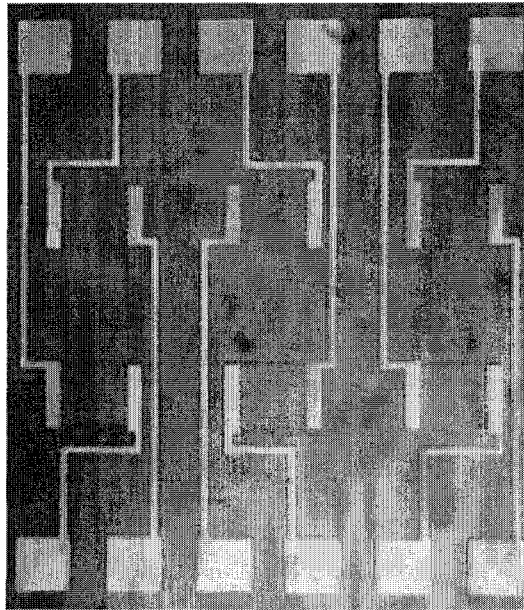


Figure 5.2- Photographs of $2.5\mu\text{m}$ width and spacing MSM photodetectors

After depositing Ge, the interdigitated electrodes were patterned by lift-off lithography. For clean lift off processing, the LOR film should be thicker than the metal layer. The spinning speed of the LOR3A was 3000 rpm for duration of 30 seconds which creates a rough resist layer of

330nm. The LOR3A was then baked at 175°C for 5 minutes. The next resist layer was image resist (S1811), which was coated at 4000rpm for 30 seconds giving a thickness of about 1.1µm. The wafer was then baked for 1 minute at 100 °C and exposed for 22 seconds with mask no. CU184-02, and then developed in MF321 for 1.5 minutes. The wafers were then transferred into a Technics Planar Etch II plasma etcher to clean away any remaining photoresist before metal deposition. The plasma etch was performed for a total of 1 minute in O₂ at a pressure of 0.3 Torr and a power of 100W. Al was then evaporated with a base pressure of 8×10⁻⁶ Torr. Thickness of Al was 200nm that was thinner than LOR thickness of 330nm. LOR was then removed with microposit remover 1165. The 1165 LOR remover removes the LOR with the layers on top and therefore only Al layer being in contact with the substrate surface will remain after removing LOR. 1165 was put in two tanks, and wafers stayed in each tank for around 30 minutes. Ultrasonic vibration was used to help improve the lift off efficiency. Figure 5.3 shows the cross section of this MSM detector.

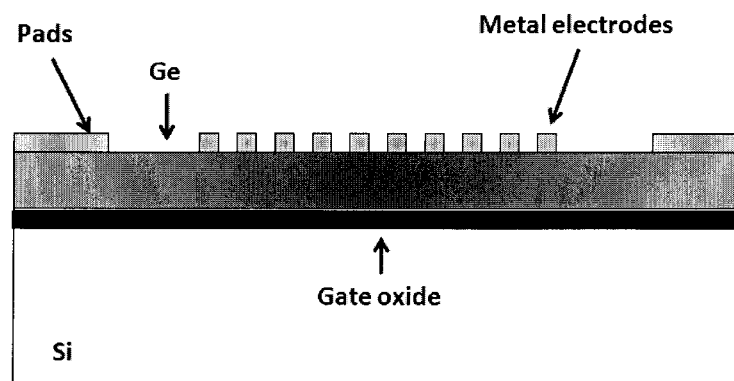


Figure 5.3- Cross section of the MSM interdigitated electrode (Metal above Ge)

As can be seen this structure is similar to conventional MSM where metal is on Ge layer, as opposed to the next section's design where metal is beneath active layer for leakage current reduction purposes.

5.1.3.2 Semiconductor on metal

Due to the surface-oriented device structure, basic performance parameters of MSM detectors are expected to be critically dependent on the surface electronic conditions. Previous investigations on GaAs MSM detectors, for example, indicate that typical performance degrading effects such as low-frequency photocurrent gain and excessive leakage current are likely to be caused by surface traps [68]. Furthermore the origin of leaky characteristics of Schottky diodes on p-GaN is suggested to be due to surface layer which gives rise to tunnelling current across the Schottky barrier [69]. C. T. Lee et al [16] have suggested that oxidation of GaAs MSM-PDs will reduce the leakage current by reduction of surface states that will also help to decrease the probability of surface breakdown. In this project, in order to reduce surface effects of the Ge active layer and reduce leakage current, a new structure is suggested. In this design the metal electrodes are on the surface of substrate, and Ge active layer is deposited on top of metal electrodes. In this case the metal electrodes are in touch with the bottom surface of Ge that should be smoother and cleaner than a thick Ge film, and expectations are dark current reduction by reducing surface effects. To have Ge on top of metal electrodes, a window was opened on the electrode pads for probing purposes. Therefore for this structure 2 masks were designed. CU294-A1 and CU294-A2 are the mask numbers for metal electrodes and MSM active layer patterning respectively. Figure 5.4 shows the designed mask using L-Edit. As can be seen there are two different dimensions of interdigitated electrodes. The smaller structure is $5\mu\text{m}$

width and spacing interdigitated electrodes with area size of $95\mu\text{m}\times 110\mu\text{m}$, while the larger structure is $10\mu\text{m}$ width and spacing interdigitated electrodes with area size of $195\mu\text{m}\times 190\mu\text{m}$. Furthermore, in order to compare the results to the previous metal dot results, $100\mu\text{m}$ diameter dots were included in the design on top side of the mask. Moreover, there is an ohmic metal electrode ring around the mask (The reason it is ohmic is that this ring has a large area of contact with the semiconductor and therefore it draws a lot of leakage current so that the device most likely has ohmic characteristics). This ohmic ring along with the dots on the right top corner was originally designed to have an ohmic junction for finding forward bias characteristics of a Schottky diode. The dots on the right top corner are surrounded with metal and gaps of 2μ , 4μ and 8μ in between. Gaps with different sizes were considered to see how the junction characteristics changes. Expectations were to see higher leakage current for lower gaps.

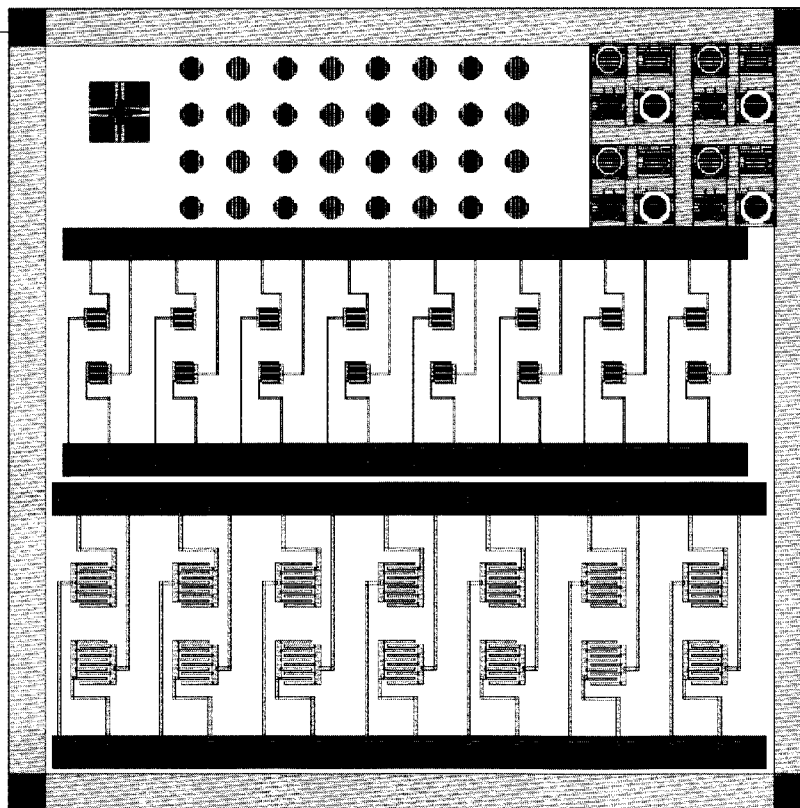


Figure 5.4- Mask design of second structure

Fabrication lithography process was pattern and etch rather than lift off, because in this design Ge is on top of Al metal and lift off patterning Al may cause damage to the Ge film.

500nm Al metal was evaporated on 1-10 Ω sheet resistance Si wafers with 0.1 μ m thick gate oxide layers. The HMDS adhesion layer was spin coated with spin speed of 4000 rpm for 30 seconds. Then after 1 minute soft bake at 100°C, S1811 was spin coated with 4000 rpm for 30 seconds and it was soft baked for 1 minute at 100°C. The wafer was then exposed for 25 seconds and then developed in MF321 for 1 minute. The sample was then hard baked at 125°C for 3 minutes. For removing the residual photoresist, the sample was put in plasma etcher for 1 minute at a power of 100w and O₂ pressure of 0.3 Torr. To etch away Al, phosphoric acid was used and it usually took about 2 minute to etch it completely. The sample was rinsed for about 10 minutes for making sure there is no phosphoric acid left. Finally to remove the photoresist the sample was put in plasma preen microwave for 5+5+5 minutes.

After the Al electrodes were patterned, the Ge active layer was sputter deposited in Varian sputter deposition system. The lithography steps are the same as Al patterning steps, however the etchant of Ge is different than that of Al. After several tries on finding an etchant and etching period for Ge, it was etched with fresh polyetch for 75 seconds. Etching Ge was the most critical process step in fabricating the sample since polyetch etches Al too, and it was important to find an optimum etching time which would etch Ge away but not the AL underneath. 75 second etching time is for a fresh polyetch and it can be longer for used polyetch. Figure 5.5 and Figure 5.6 show the cross section of this design and top view of the fabricated device respectively.

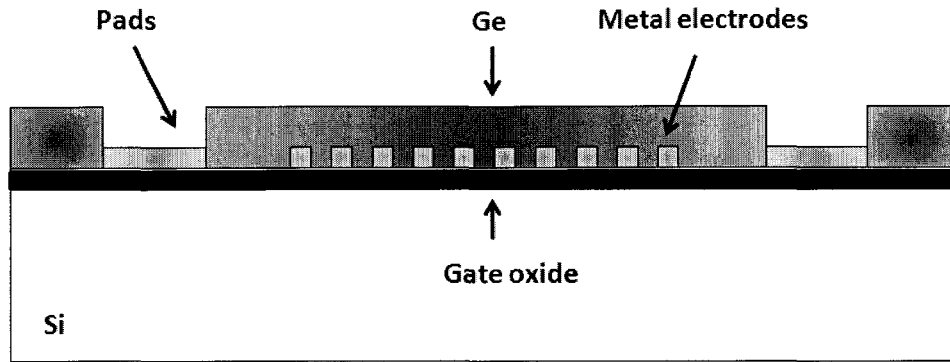


Figure 5.5- Cross section of the second MSM interdigitated electrode design (Ge above metal electrodes)

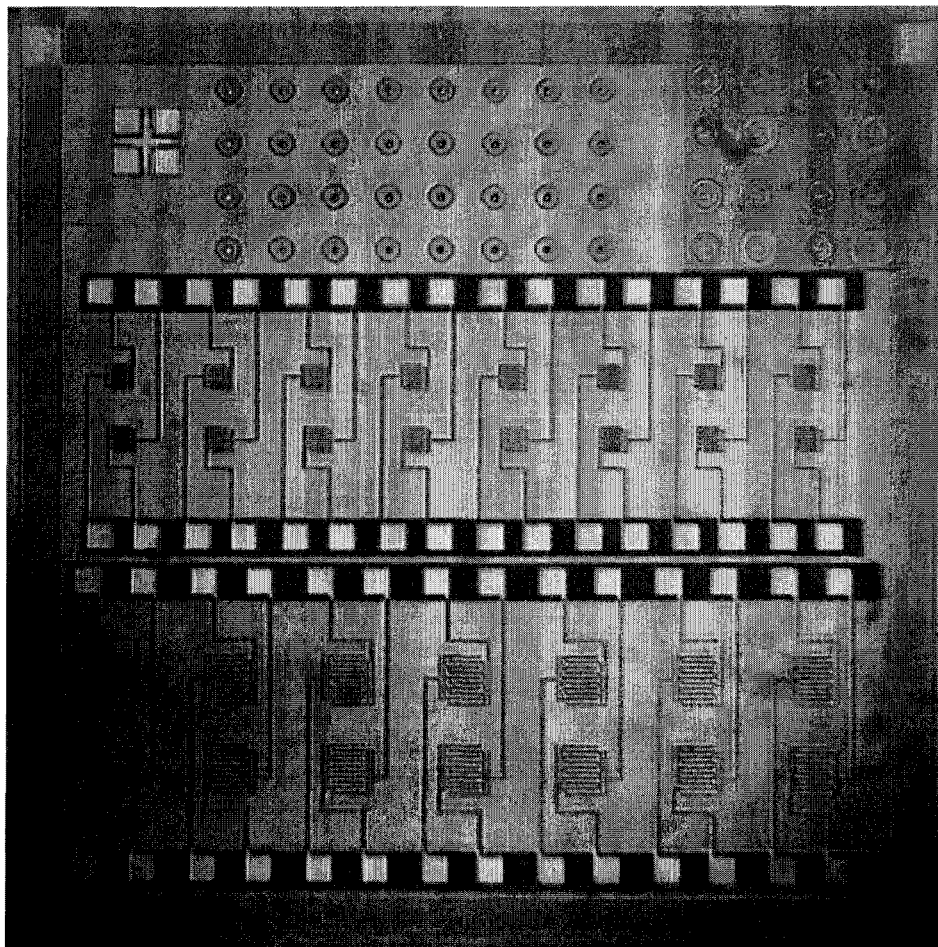


Figure 5.6 – Picture of the fabricated sensors on the same chip

Sample 13, 15, and 16 were fabricated with the same fabrication process and deposition conditions. Sample 13 and 15 were exactly the same and it was to make sure we get the same

results with the same deposition conditions. To find different hydrogen concentration effects in the film, sample 17, 19 and 21 were deposited with 15%, 25%, and 10% hydrogen gas diluted in Ar plasma gas respectively. Table 5.1 shows the summary of all of the samples' descriptions. However; for simplicity reasons, other system parameters such as RF power is not included in this table which can be found in Table 4.3.

<i>Sample no</i>	<i>MSM structure</i>	<i>Metal location</i>	<i>Metal</i>	<i>Substrate</i>	<i>Ge dep. Gas & flow rate</i>	<i>Location on chuck</i>	<i>Comment</i>
3	Dots	Above Ge	Al	Gate oxide Si	Ar	Center	-
4	Dots	Above Ge	Ti	Gate oxide Si	Ar	Center	-
5	Dots	Above Ge	Al	Gate oxide Si	5%H ₂ /Ar	Center	-
6	Dots	Above Ge	C	Single cryst. Ge	NA	Center	-
7	Dots	Above Ge	Au	Single cryst. Ge	NA	Center	-
8	Dots	Above Ge	Al	Gate oxide Si	Ar	Center	-
9	Dots	Above Ge	Al	Gate oxide Si	Ar	Center	-
10	Dots	Above Ge	Al	Gate oxide Si	5%H ₂ /Ar	Center	-
11	Dots	Above Ge	Al	Gate oxide Si	Ar	Center	-
12	Interdigitated electrodes	Above Ge	Al	Gate oxide Si	5%H ₂ /Ar	Side	-
13	Interdigitated electrodes	Under Ge	Al	Gate oxide Si	5%H ₂ /Ar	Side	-
14	Interdigitated electrodes	Under Ge	Al	Gate oxide Si	5%H ₂ /Ar	Center	-
15	Interdigitated electrodes	Under Ge	Al	Gate oxide Si	5%H ₂ /Ar	Side	-
17	Interdigitated electrodes	Under Ge	Al	Gate oxide Si	25%H ₂ /Ar@27.7sccm Ar@18.7sccm	Side	15% H ₂
18	Interdigitated electrodes	Under Ge	Al	Gate oxide Si	25%H ₂ /Ar@25sccm	Center	25% H ₂
19	Interdigitated electrodes	Under Ge	Al	Gate oxide Si	25%H ₂ /Ar@25sccm	Side	25% H ₂
21	Interdigitated electrodes	Under Ge	Al	Gate oxide Si	25%H ₂ /Ar@29 sccm Ar@12.5sccm	Side	10% H ₂

Table 5.1 - Photodetector sample descriptions

Note that system parameters of sample 9-11 are mentioned in previous chapter, and all of the other samples have same system parameters as sample 3.

5.2 Characterization

5.2.1 Dark current

Dark current measurements were done in order to find the Schottky characteristics of the junctions and leakage current of the detectors. This measurement was taken with Hewlett Packard 4155A Semiconductor parameter analyzer at Carleton University.

5.2.1.1 C-V dots

Two probes were landed on each dot to measure I-V characteristics of the device as is shown in Figure 5.1. Dark current measurement of samples 3, 4, 5, 8, 9, and 10 are shown in bellow.

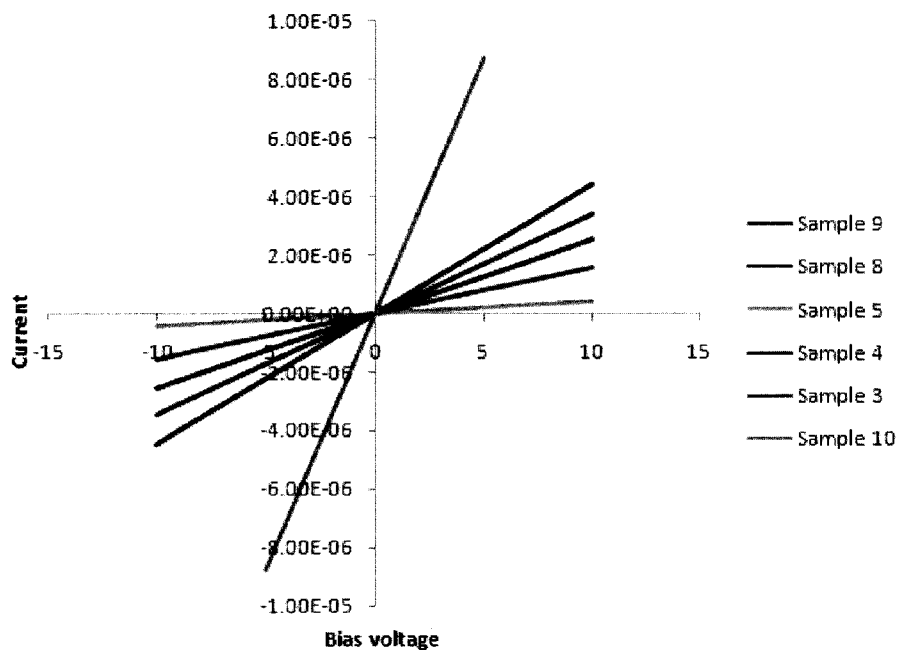


Figure 5.7- I-V characteristics of Sample 3, 4, 5, 8, 9, and 10

As can be seen all the above samples show ohmic I-V characteristics. That is because all the samples have the 1.8mm radius dots as the contact metal structure which are quite big in size and therefore they draw a lot of leakage current and the junction is more likely to be ohmic rather than schottky. As it is already discussed in previous chapter, sample 5 has the lowest leakage current and therefore hydrogenating Ge was found to help reducing the leakage current. The reason is that hydrogen forms Ge-H with dangling bonds or weak bonds and therefore reducing the amount of defects in the film, leading to lower dark current. In order to see a Schottky diode's characteristics rather than an MSM detector, a dot (Schottky diode) was probed with the ohmic ring to verify diode characteristics. However since the window opened on the dots for probing reasons was too little, it was not easy to get a clear response out of it, but unexpectedly a symmetric response in I-V characteristics was seen while a non symmetric response was expected.

5.2.1.2 Metal electrode effects

Figure 5.8 shows the I-V results of Al (Sample 6), and Au (Sample 7) on Single crystalline Ge wafer. As can be seen, Al is found to show lower leakage current which makes it a better metal electrode candidate compared to Au. That might be because the work function of Al with c-Ge leads to higher barrier height and therefore lower leakage current.

The single crystalline Ge with the metal dots shows non-ohmic characteristics, however the I-V behaviour is not similar to an ideal diode. As can be seen, the current does not saturate and it keeps increasing with the bias voltage. The reason is that the doping concentration of c-Ge wafer is relatively high. This experiment was done on this rather higher doped Ge wafer because of the availability and timing issues. Although the Ge wafer has crystalline structure, but the leakage

current has increased to a large amount compared to the sputter deposited a-Ge. That might be because of the high doping of Ge wafer (.005-.02 ohms/cm), and the leakage current might decrease at lower doping levels. The future work here is to compare dark current and photocurrent characteristics of a-Ge:H with lower doped single crystalline Ge, and poly crystalline Ge, to more precisely investigate material characteristics.

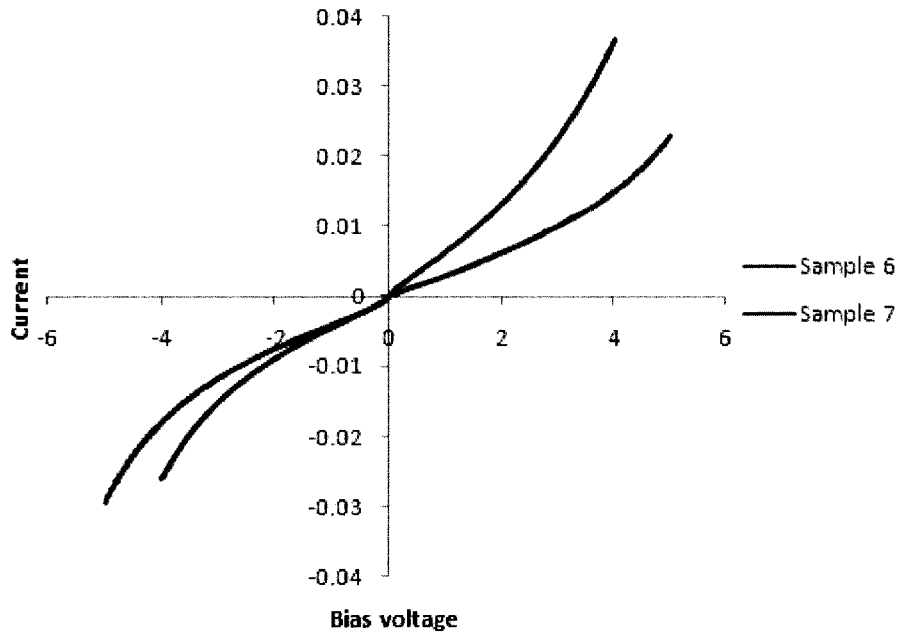


Figure 5.8- I-V Characteristics of metal on Single crystalline Ge samples

The reverse bias characteristics of the back to back schottky contacts can be evaluated by ideality factor(n) and reverse leakage current (I_0) of the junction [55]. As previously mentioned in chapter 3, plot of $\ln\left(\frac{I \exp(qV/kT)}{(\exp(qV/kT)-1)}\right)$ versus V is just a linear line and the slope of the line is equal to q/nkT , from where the quality factor of the Schottky diode can be calculated. This plot is shown in Figure 5.9 for sample 6. Extrapolation of the plot at $V=0$ gives out saturation current [55].

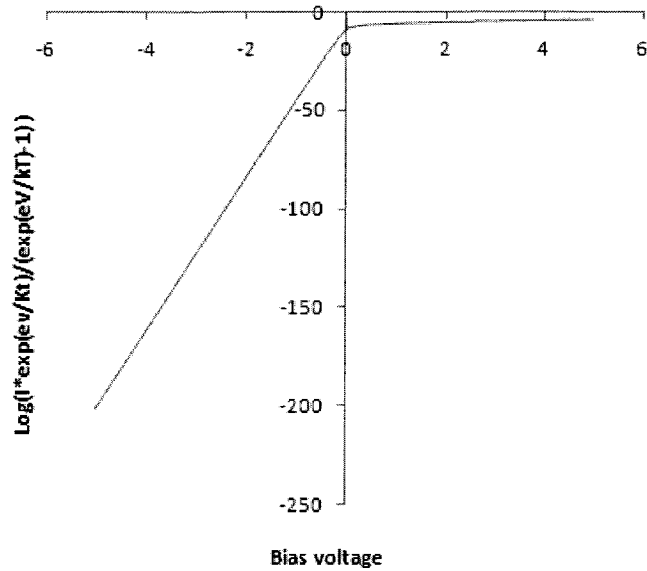


Figure 5.9- Logarithmic plot of $\left(\frac{I \exp(qV/kT)}{(\exp(qV/kT)-1)}\right)$ versus V of sample 6 at 293K

From above quality factor is found to be 1.14 that is not close to ideal (1.03 [55]), and the saturation current is $\ln(I_0) \sim -2.5 \rightarrow I_0 = 82 \text{mA}$, and from equation (3.17) the barrier height is found to be:

$$= \frac{1.38 \times 10^{-23} \times 293}{1.6 \times 10^{-19}} \times \ln\left(\frac{26.4 \times \pi \times (1.8 \times 10^{-3})^2 \times 293^2}{82 \times 10^{-3} \text{A}}\right) = 0.143 \text{eV}$$

As can be seen, the barrier height is too low which causes a lot of leakage current draw. I-V characteristic of the device shows a soft break down of the barrier height, and therefore the current starts to increase and it never saturates. For that reason, the barrier heights of the samples with similar characteristic will be calculated based on the current at 5 volts.

5.2.1.3 Interdigitated electrodes

So far the I-V characteristics of the MSM detectors with metal dots were discussed. I-V characteristics of the interdigitated electrodes that are the main structure of MSM detectors in this project are discussed in this section.

All the interdigitated MSM-PDs showed similar I-V curves, however the leakage current and barrier height of each sample was different. Sample 13's I-V curves are shown in Figure 5.10.

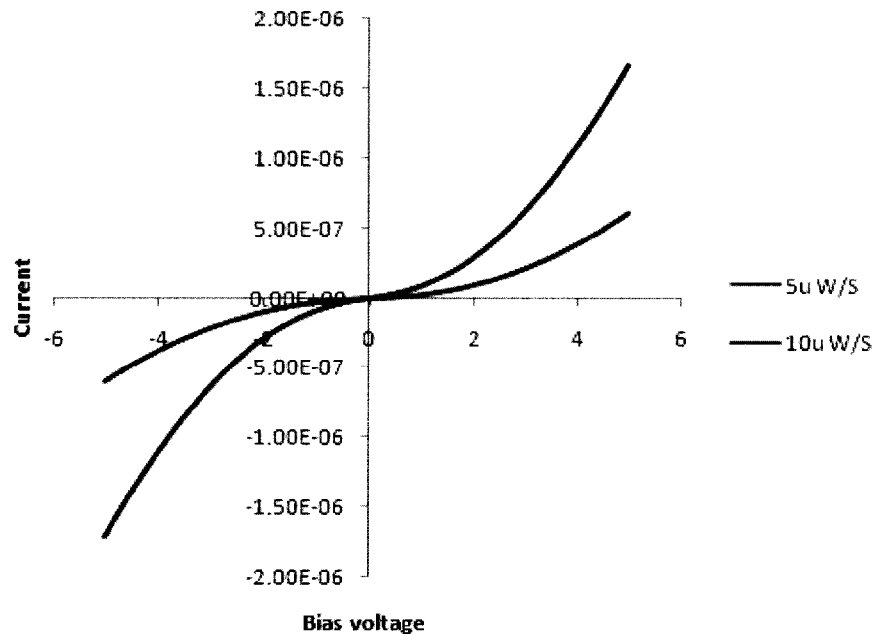


Figure 5.10- Sample 13 interdigitated electrode I-V characteristics for 5u, and 10u width/spacing electrodes

This figure shows that the 10 μ m width/spacing interdigitated electrodes have higher leakage current than 5 μ m width/spacing structure. This is because the device has almost twice area as the 5 μ m width/spacing structure leading to higher leakage current. Furthermore, this figure shows that the I-V characteristics of the junctions have deviated from the ideal I-V characteristics. According to Li M. [70], this is because of a soft break down shown in the I-V characteristics that might be due to large amount of interface states within the film leading to an increase the

leakage current. Figure 5.11 and Figure 5.12 show the MSM I-V characteristics of their work. They report on Si based MSM diodes operating at 800nm, enhancing a-Si:H layer on c-Si, as well as SiO₂ passivation layer to help reducing the dark current. They have designed 50um width and spacing as well as 4u width and spacing interdigitated electrodes. Figure 5.11 (a) and (b) shows dark and photo current I-V characteristics of 50u width and spacing device, and Figure 5.12 (a) and (b) shows dark current and photocurrent I-V characteristics of 4u width and spacing device without a-Si:H layer.

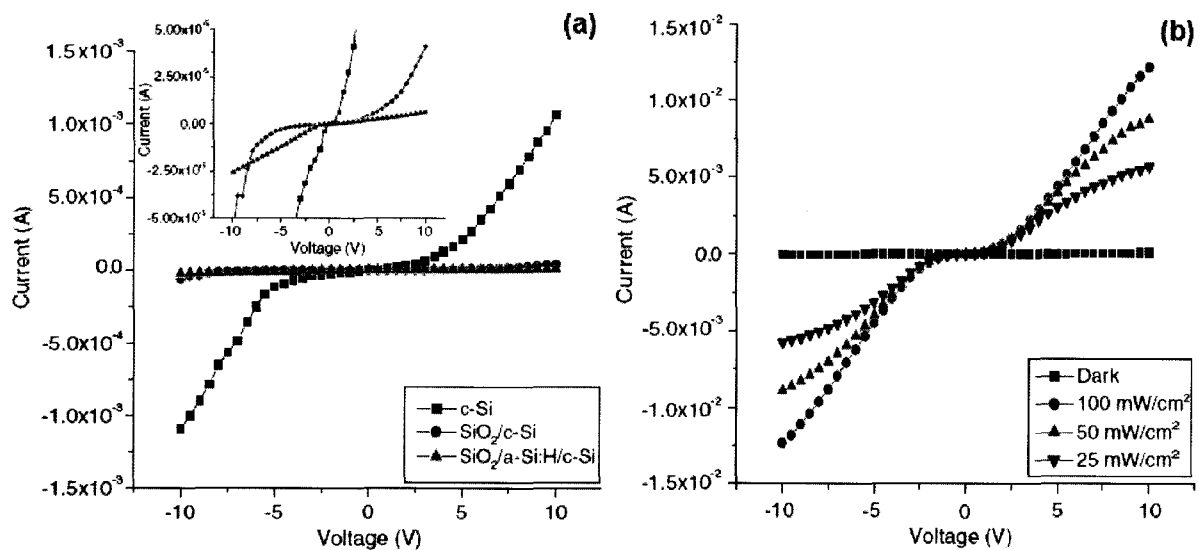


Figure 5.11- I-V characteristics of MSM photodiode with Cr metallization and 50u width and spacing (a) Dark current with different substrates (b) photocurrent of SiO₂/a-Si:H/p-Si at different ranges of power [70]

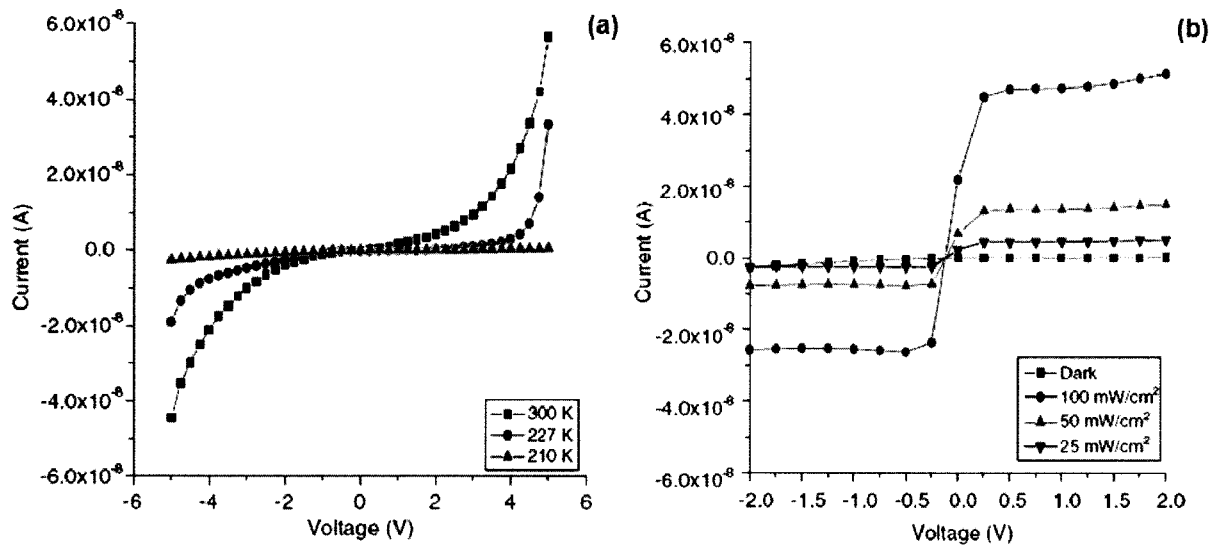


Figure 5.12- I-V characteristics of SiO₂/n-Si MSM photodiode with Pd metallization and 4u width and spacing (a)Dark current at different temperatures (b) photocurrent at 227°k [70]

As can be seen they are having similar MSM detector behaviour with the results from this work.

Since the samples with MSM interdigitated electrodes show similar dark current characteristics, only sample 13's I-V curves are shown and the ideality factor, and leakage current of all other samples are summarized in Table 5.2.

Wafer No.	Dimension(w/s)	Area size (μm) ²	Number of electrodes	Current @ - 5v	n	$\Delta\phi(\text{eV})$
12	2.5/2.5 μm	100×100	19	-170 μA	1.1815	-
13	5/5 μm	95×110	10	-0.7 μA	1.1739	0.26
15	5/5 μm	95×110	10	-0.58 μA	1.1480	0.26
17	5/5 μm	95×110	10	-7.96 μA	1.1680	0.194
19	5/5 μm	95×110	10	-11.6 μA	1.16	0.185
21	5/5 μm	95×110	10	-7.72 μA	1.1638	0.2
13	10/10 μm	190×195	10	-1.9 μA	1.1938	0.25
15	10/10 μm	190×195	10	-2.18 μA	1.1651	0.25
17	10/10 μm	190×195	10	-17 μA	1.1520	0.195
19	10/10 μm	190×195	10	-28.4 μA	1.1616	0.18
21	10/10 μm	190×195	10	-15.7 μA	1.1635	0.2

Table 5.2- Ideality factor and dark current of the interdigitated MSM photodetectors

As can be seen from table above, with the new device design of Ge on metal electrodes, the current density has reduced from $17 \text{ nA}/(\mu\text{m})^2$ (sample 12) to $0.064 \text{ nA}/(\mu\text{m})^2$ (sample 13). Therefore this new design has lead to dark current reduction by a large amount. M. Shahin et al. [71] has reported on dark I-V characteristics of n^+ LP-CVD deposited a-Si:H with Pt metal schottky contact. I-V characteristic show higher leakage current diodes compared to the sputtered a-Ge:H MSMs that are fabricated in this project.

Ideality factor of the diodes is not close to ideal that is 1.03. Ideality factors bellow 1.1 are usually considered good schottky contacts [72]. Higher ideality factor means the tunnelling current is increasing and it will be more dominant [51]. The reason might be because of high amount of defects within the film, surface recombination, and thermally activated electron-hole pairs that significantly affect Schottky barriers. However these values show better schottky characteristics than Au on RF sputtered a-Ge:H film having ideality factor equal to 2 [73]. Figure 5.13 shows the leakage current versus barrier height of the above samples.

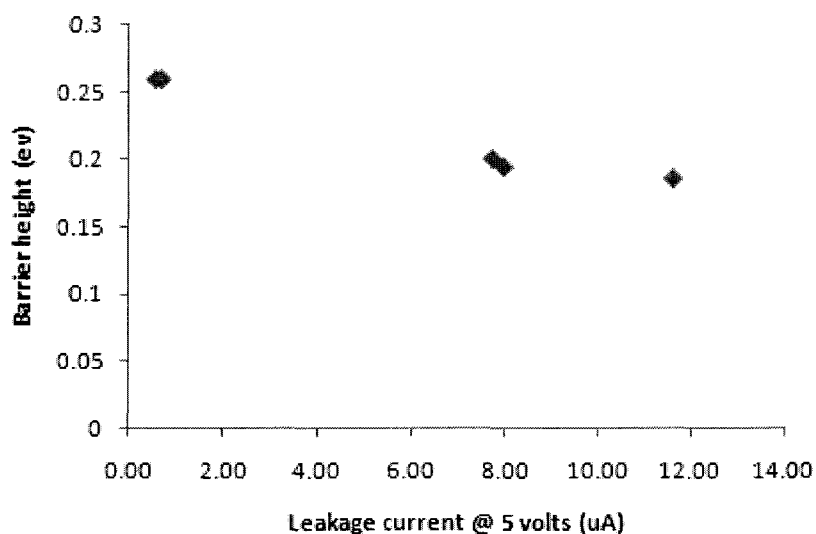


Figure 5.13 – Barrier height VS leakage current of devices with same electrode area size ($95\mu\text{m}\times 110\mu\text{m}$)

The barrier heights are generally low. Schottky contacts grown on bulk Ge (111) show barrier height of 0.44eV for sputtered Au [74]. As it was already discussed in section 5.2.1.2, barrier height is calculated by finding saturation current from the $\left(\frac{I \exp(qV/kT)}{(\exp(qV/kT)-1)}\right)$ versus V plot by intercepting the straight line to $v = 0$, and fitting it into expression (3.17), which is $\varphi = \frac{kT}{q} \ln \left(\frac{A^* S T^2}{I_0}\right)$. However, since the current never saturates in the I-V curves of the samples (which is due to the soft breaking down of the junction), it was not possible to make an extrapolation to $v = 0$, and therefore the $\ln \left(\frac{I \exp(qV/kT)}{(\exp(qV/kT)-1)}\right) = \ln(I_0)$ was taken at 5 volts. It should be noted that in the entire barrier height calculations, A^* is 26.4 [50], with the temperature being 293K.

As can be seen, sample 13 and 15 have the same barrier height since these samples were fabricated with the same process to make sure the results are not different. Furthermore, barrier heights of the same sample but different electrode size are similar that shows the leakage current density of these devices are the same. Sample 15, sample 21, sample 17, and sample 19 have hydrogen concentrations of 5%, 10%, 15%, and 20%, and barrier heights of 0.26, 0.2, 0.194, and 0.185eV respectively. This shows that as the hydrogen concentration increases, saturation current increases, meaning the barrier height has decreased. The reason of saturation current increase is discussed in the next section. Exact electrode area of sample 12 was not known, and therefore barrier height could not be calculated.

5.2.1.4 Hydrogenation effects

Hydrogen plays an important role in reducing dark current. As it was seen in the previous sections, increasing H₂ concentration from zero to 5% in the plasma reduces the dark current. In

order for more dark current reduction, higher amount of H₂ was used to deposit Ge. Figure 5.14 shows the different hydrogen concentrations and the leakage currents.

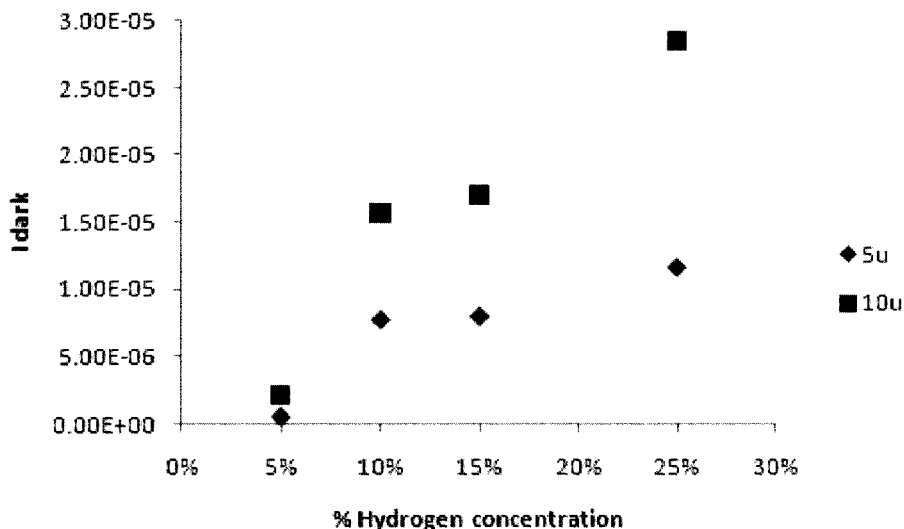


Figure 5.14- Dark current at different hydrogen concentrations

This figure shows that more hydrogenation of the films had opposite effect and the dark current increased. That might be because H₂ lowers the amount of defects, leading to higher lifetime of carriers that are sources of dark current (e.g. thermally activated carriers), and therefore increasing the amount of dark current. From the above results it can be seen that there is an optimum hydrogen concentration for minimum leakage current and this amount was 5% between these samples.

5.2.2 Photoresponse

Photoresponse measurements were taken at Carleton University using a continuous wave laser diode operating at 1505 nm which provides a good indication of performance at 1.550 μ m of communication wavelength. Figure 5.15 shows the set up for optical response measurement. The laser output power from the end of the single-mode fiber was around 2.8mW. The DC current

output versus bias voltage was monitored with Hewlett Packard 4155A Semiconductor parameter analyzer. A glass capillary was attached to the end of fiber and the optical fiber was held with a probe for positioning purposes. Only the MSM interdigitated photodetector sensors were characterized for their photoresponsivity.

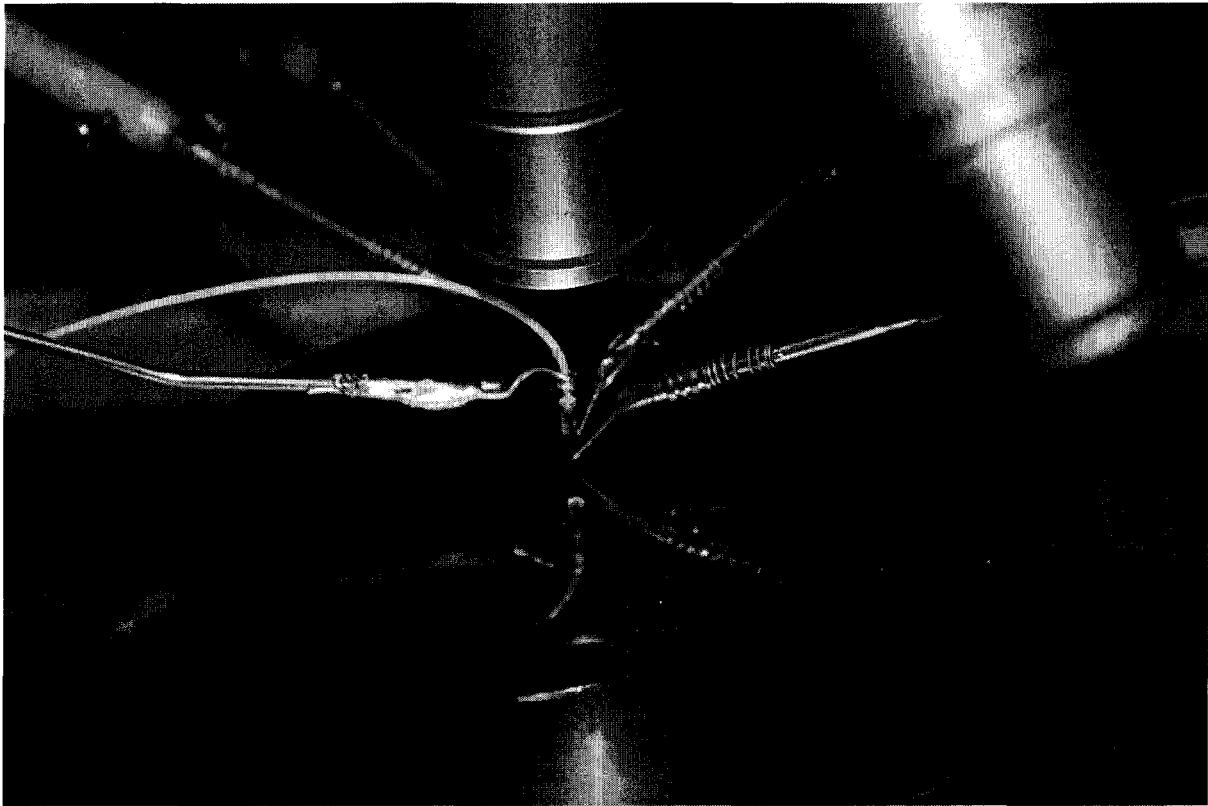


Figure 5.15- Optical response measurement set up

In order to find the responsivity, the ratio of $\frac{\text{Beam area}}{\text{Detector area}}$ was found for finding the amount of power incident on the detector area. The fiber was about 2 millimetres higher than the surface of the chip during the measurements and the beam diameter at 2 mm was found to be about $500\mu\text{m}$; however diameter of the beam right out of the capillary was measured to be $100\mu\text{m}$ (Numerical aperture $NA \cong 0.10$).

5.2.2.1 Metal on semiconductor

Time response of the sensor at 5v bias was measured with the parameter analyzer. The voltage applied on the photodetector was 5v all the time during the measurement and behaviour of dark and photo current with time were investigated. There is an initial transient in the current and a drift during the measurement, however this is a small fraction of the total current and may be related to transient characteristics of the 4145 SPA. The fiber was aligned on the chip so that the highest photoresponse was achieved. Figure 5.16 shows the results for sample 12.

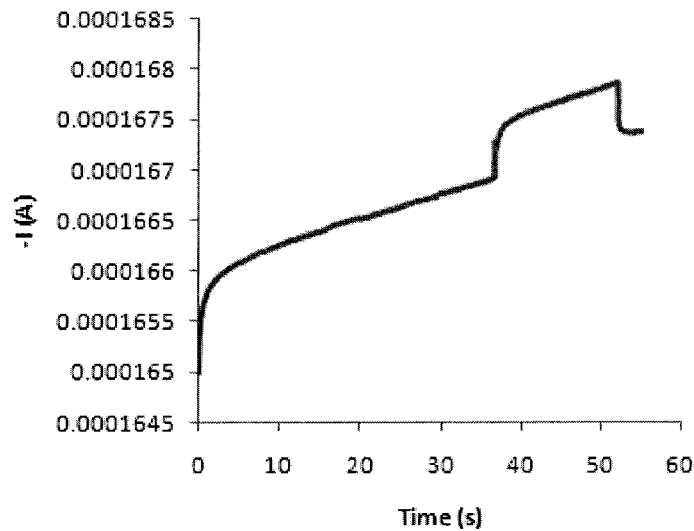


Figure 5.16 – Transient response of sample 12

The pulse shows response of the detector to the 1505 μm laser diode with input power of about 2.8mW. As can be seen, initially the power was off, but when the laser diode turned on, the current increased, and when again the power was turned off, current decreased to its initial value. That is because the photons generate electron and hole pairs which contribute to higher current. I_{Photo} which is the difference between the total photo-current and the dark current is 350nA, leading to a photoresponse of:

$$\mathcal{R}_{Sample\ 12} = \frac{I_{photo}}{P_o} \times \frac{Beam\ area}{Detector\ area} = \frac{350nA}{2.8mW} \times \frac{\pi \times (250\mu m)^2}{100\mu m \times 100\mu m} = 2.5mA/w$$

Since the IR beam area was larger than detector area, responsivity is multiplied by the ratio of beam area/detector area.

Responsivity can also be measured by doing a laser diode power sweep and the slope giving the responsivity, but we confined the measurements to the above tests.

5.2.2.2 Semiconductor on metal

Figure 5.17 shows the response of the 10 μm width/spacing MSM electrodes of sample 15, 21, 17, and 19.

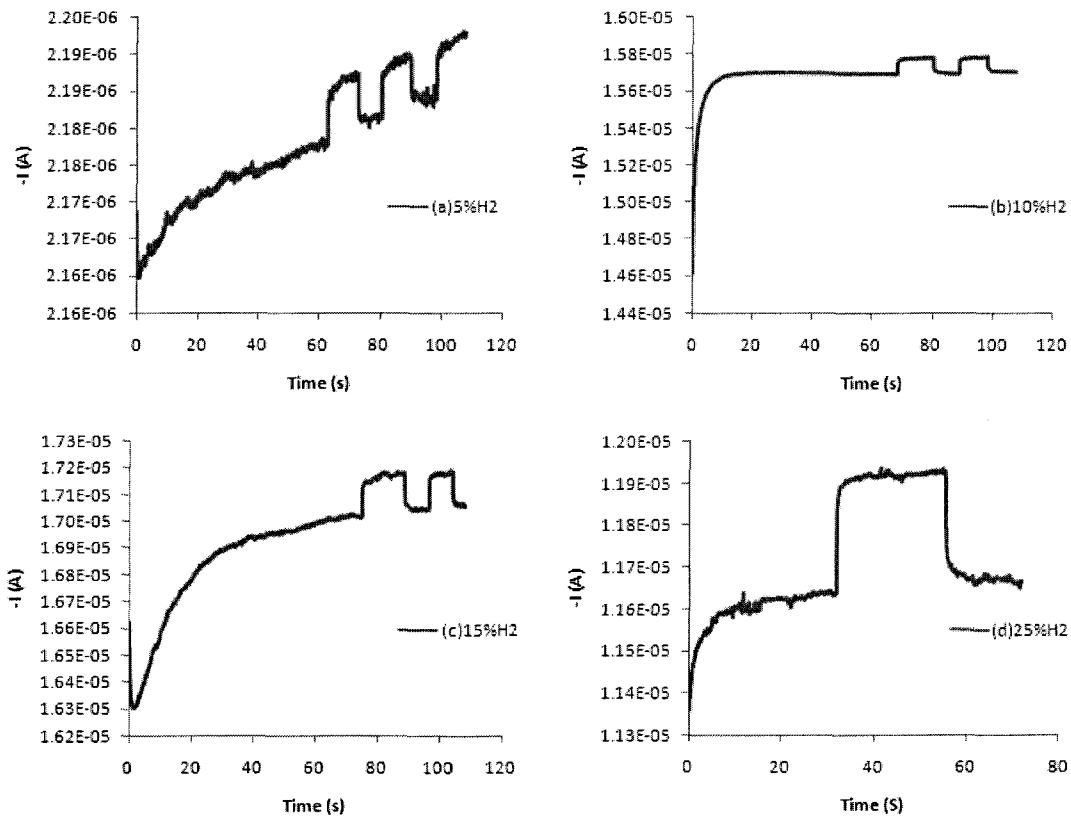


Figure 5.17- Photoresponse of sample 15(a), 21(b), 17(c), and 19(d)

I_{Photo} and photo-responsivity values for the 2.5 μm width/spacing, 5 μm width/spacing, and 10 μm width/spacing MSM-PDs are summarized in Table 5.3.

Sample no.	%H ₂	Electrode width/Spacing	Area (μm) ²	I_{Dark}	I_{Photo}	Photoresponse (mA/w)	$I_{\text{Photo}}/I_{\text{Dark}}$ ($\times 10^{-3}$)
12	5%	2.5	100×100	170 μA	350nA	2.5	2.05
15	5%	5	95×110	0.58 μA	None	0	0
21	10%	5	95×110	7.72 μA	20nA	0.1342	2.6
17	15%	5	95×110	7.96 μA	40nA	0.26842	5.03
19	25%	5	95×110	11.6 μA	300nA	2	26
15	5%	10	190×195	2.18 μA	7nA	0.013	3.2
21	10%	10	190×195	15.7 μA	80nA	0.15	5.1
17	15%	10	190×195	17 μA	120nA	0.227	7.06
19	25%	10	190×195	28.4 μA	600nA	1.1	21.1

Table 5.3- Photoresponse of the sensors with different hydrogen concentration

As can be seen from the above table, sample 12 has the highest photoresponse; however it has the highest dark current among other samples. J. Liu [41] has worked on polysilicon MSM detectors having responsivity value of 0.3 mA/W which has 4 times less photoresponse, but the leakage current is quite lower (40 μA at 10v) compared to this device (170 μA at 5v). Although sample 12 has the highest photoresponse, but its high leakage current reduces its performance. The performance is somehow shown by current ratio in the last column of Table 5.3. This ratio shows that the best current ratio belongs to sample 19 with detectors of 5 μm width/spacing electrodes. As can be seen, the leakage current is 11.6 μA and photoresponse for this device is 2mA/W. The reason of dark current reduction is that since this new structure has the semiconductor to be on top of metal electrodes, the surface effects of the semiconductor are removed, and therefore leading to lower leakage current.

While higher photoresponsivity was expected in semiconductor on metal samples because of no light reflection and blocking by electrodes at the surface of semiconductors, this device shows lower photoresponse. This might be due to two different reasons. First one is that both sample 12 and sample 15, have device area of about 100 μm \times 100 μm , but sample 12 has 19 interdigitated

electrodes of $2.5\mu\text{m}$ width/spacing, while sample 15 has only 10 interdigitated electrodes of $5\mu\text{m}$ width/spacing. Having lower spacing between the electrodes, but more number of electrodes will increase the probability of photo-carrier collection by the electrodes (since the photo-carriers will be generated in the higher electric field) while higher spacing between the electrodes with fewer number of interdigitated electrodes increases the probability of photo-carrier recombination. The second reason is that in sample 15, the thickness of the Ge active layer might be high (in this case it is $2\mu\text{m}$), so that some photo-generated carriers recombine before reaching to the bottom metal electrodes. The film thickness of Ge to absorb 90% of light is calculated to be $0.1\mu\text{m}$ from $x = \frac{\ln(90\%)}{\alpha}$, where α is the absorption coefficient of Ge. Therefore, many photo-generated might recombine since the absorption length is very lower than film thickness.

Therefore to improve this structure in the future, reducing finger width and spacing (with the same area size), and also reducing the thickness of the active layer will help overall better performance of the detector. Samples with higher hydrogen concentrations show higher photoresponse because of hydrogen incorporation in the film. This effect is discussed in the next section.

5.2.2.3 Hydrogenation effects

Figure 5.18 shows the photocurrent versus hydrogen concentration of the samples.

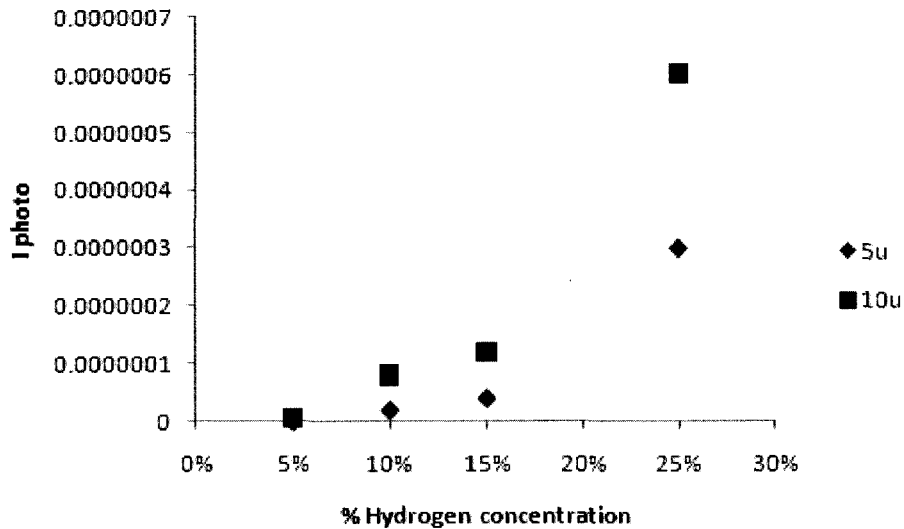


Figure 5.18-Photocurrent at different hydrogen concentrations

As can be seen, as the hydrogen concentration increases, photocurrent also increases. That is because H_2 forms Ge-H bonds with dangling bonds and with the defects, and therefore decreases the amount of defects which leads to lower trapping of photo-carriers and therefore higher photocurrent. However the percentage of hydrogen concentrated in the films is not the same as plasma gas, and the films should be characterized in order to find out the percentage of H_2 within the film. FTIR measurements can help identifying the peaks on the IR spectrum and then deriving the hydrogen concentration from the IR spectra results [75].

Deposition temperature of $450^\circ C$ is considered a high temperature for H_2 , since hydrogen atoms will not easily make Ge-H bonds with Ge atoms at this high temperature. It has been reported that at high temperatures of $450^\circ C$, almost no hydrogen will remain in the amorphous silicon

[42]. Therefore the performance of these devices may be improved by reducing the temperature to lower degrees.

5.3 Conclusion

Different MSM structures were fabricated and characterized for their dark current and photoresponsivity. Metal-on-semiconductor MSM interdigitated electrode (sample 12) with device area of $100\mu\text{m}\times 100\mu\text{m}$ showed highest responsivity of 2.5 mA/W at 5volts. This was the highest photoresponse achieved between other detectors; however this device showed highest dark current of $170\mu\text{A}$ amongst other devices, reducing the device performance. Semiconductor-on-metal structures, on the other hand, showed lower dark currents due to surface effect reduction of the semiconductor. Highest photoresponsivity achieved with this structure is 2mA/W at 5volts that belongs to highest hydrogen concentration sample with device area of $95\mu\text{m}\times 110\mu\text{m}$ and $5\mu\text{m}$ width/spacing metal electrodes. Dark current of this device was as low as $11.6\mu\text{A}$, showing overall better performance compared to metal-on- semiconductor structure.

Chapter 6

Conclusion and recommendations

6.1 Conclusion

This thesis describes research on RF sputtered germanium-based MSM detectors as well as their design, fabrication, and characterization. Different Ge films were deposited with different system parameters and they were characterized based on crystal structure and resistivity of the films. It was found that RF power of 200W gave highest resistivity between films prepared with 100W and 40W RF powers since there were lower amount of defects involved in the films, leading to lower dark current. Furthermore, films deposited under and 450°C and 250°C showed rather amorphous crystalline structure based on XRD spectra. Temperature of 450°C was chosen as the deposition temperature for all other samples because generally higher deposition temperatures show better crystalline structure.

Amorphous germanium hydrogenated films were also investigated in this thesis. It was shown that hydrogenation of films increases photoresponse since hydrogen reduces the amount of localized states and therefore life time of the carriers increases. Hydrogen concentrations of 0%, 5%, 10%, 15%, and 25% in the plasma also showed that 5% hydrogenated film had lowest leakage current among the 4 other samples. That is because at 0% H₂ there are too many defects within the film and these defects increase the amount of leakage current. While hydrogen decreases the amount of defects by making Ge-H with dangling bonds, higher concentrations can increase life time of dark current carriers (for example thermally generated carriers). In this work, within the same MSM structure, 25% H₂ deposited films with area of 95μm by 110μm

showed highest photoresponse of 2mA/W and leakage current of 11.6 μ A at 5 volts. 5% H₂ films showed lowest leakage current of 0.58 μ A at 5 volts for device area of 95 μ m by 110 μ m, however this device showed no photoresponse.

It was also shown that surface states affect the characteristics of metal-semiconductor junction by depositing semiconductor on metal, opposing conventional metal-on-semiconductor MSM designs. This design helped reducing surface effects of the semiconductor and therefore the leakage current from 170 μ A for device area of 100 μ m by 100 μ m (sample 12) to 0.58 μ A for device area of 95 μ m by 110 μ m at 5v (Sample 15). Since the electrodes are beneath Ge, there is no light reflection by the metal electrodes at the surface of semiconductor and the photoresponse is expected to be increasing in this design. However, photoresponsivity unexpectedly decreases.

Photoresponse reduction might be because of two reasons. First, the generated electron-hole pairs near the surface are more probable to recombine until they are collected by the electrodes underneath Ge, and second, having more electrodes within the same device area increases the probability of carrier collection by the electrodes (2.5 μ m width/spacing (sample 12) compared to 5 μ m width/spacing (sample 15) within 100 μ m by 100 μ m area). Since the interdigitated electrodes did not have the same width and spacing (but the same area), it was unclear whether lower responsivity was due to thickness of Ge layer or width and spacing of the electrodes.

Performance of the devices was also shown by ratio of $I_{\text{Photo}}/I_{\text{Dark}}$. The highest $I_{\text{photo}}/I_{\text{Dark}}$ belongs to sample 19 with 5 μ m width/spacing, showing hydrogenation and surface effect reduction has helped overall better performance of the device.

Having different device area of 95 μ m \times 110 μ m and 190 μ m \times 195 μ m showed that higher device area has higher photocurrent (300nA, 600nA respectively), but the leakage current is also high

($11.6\mu\text{A}$, $28.4\mu\text{A}$ respectively). The increase in photo-current and dark current was almost about twice as much in detectors with $190\mu\text{m}$ by $195\mu\text{m}$ area size.

6.2 Recommendations and future work

Further insight into material characterization is needed by having samples with more variety of deposition temperatures in order to find the best growing temperature. Having more samples with different hydrogen concentration and characterizing them for defect density will help better understanding of how hydrogen affects dark current and photocurrent characteristics.

Interdigitated MSMs can be investigated with more metal choices to find best possible metals for a-Ge:H films. Devices with better performance can be achieved by having smaller interdigitated electrode width/spacing ($2.5\mu\text{m}/2.5\mu\text{m}$ in Carleton University fabrication laboratory), with the semiconductor-on-metal design. Higher performances can also be investigated by utilizing barrier height enhancement layer or interdigitated electrodes with different anode and cathode metals electrodes.

Finally integrating the photodetector with a MEMS micromirror, the original motivation behind this project, is an important future step in this project.

References

- [1] J. D. Cressler, *Silicon Heterostructure Handbook : Materials, Fabrication, Devices, Circuits, and Applications of SiGe and Si Strained-Layer Epitaxy*. Boca Raton, FL : CRC Taylor & Francis, 2006.,
- [2] Optical Society of America - Bass, Michael. (1995, *Handbook of Optics*. (2nd Edition ed.)
- [3] H. Bach, "Ultrafast photodetectors and receiver," *Journal of Optical and Fiber Communications Research*, vol. 2, pp. 293-344, 10/01. 2005.
- [4] Wang Yin-Shu, Li Jin-Min, Wang Yu-Tian, Wang Yan-Bin and Lin Lan-Ying, "Si_{1-x}C_x alloy formation and its characteristics after carbon ion implantation in silicon," *Chinese Journal of Semiconductors*, vol. 22, pp. 979-84, 08. 2001.
- [5] L. Naval, B. Jalali, L. Gomelsky and J. M. Liu, "Optimization of Si_{1-x}Ge_x/Si waveguide photodetectors operating at $\lambda=1.3 \mu\text{m}$," *Lightwave Technology, Journal of*, vol. 14; 14, pp. 787-797, 1996.
- [6] S. Luryi, A. Kastalsky and J. C. Bean, "New infrared detector on a silicon chip," *Electron Devices, IEEE Transactions on*, vol. 31; 31, pp. 1135-1139, 1984.
- [7] P. V. Santos, C. F. Graeff and I. Chambouleyron, "Light-induced metastability in a-Ge:H," *J. Non Cryst. Solids*, vol. 128, pp. 243-54, 05. 1991.
- [8] M. Li, "Metal-semiconductor-metal photodetectors," pp. 164, 2006.
- [9] K. H. J. Buschow, R. W. Cahn, M. C. Flemings, B. Ilschner, E. J. Kramer and S. Mahajan. (2001, *Encyclopedia of Materials - Science and Technology*.
- [10] T. Sugeta, T. Urisu, S. Sakata and Y. Mizushima, "Metal-semiconductor-metal photodetector for high-speed optoelectronic circuits," in *Proceedings of the 11th Conference on Solid State Devices*, 1979, pp. 459-64.
- [11] C. W. Slayman and L. Figueroa, "Frequency and pulse response of a novel high speed interdigital surface photoconductor (IDPC)," *IEEE Electron Device Lett.*, vol. ED-2, pp. 112-14, 05. 1981.
- [12] C. J. Wei, H. -. Klein and H. Beneking, "Symmetrical MOTT barrier as a fast photodetector," *Electron. Lett.*, vol. 17, pp. 688-90, 1981.
- [13] A. K. Okyay, C. O. Chui and K. C. Saraswat, "Leakage suppression by asymmetric area electrodes in metal-semiconductor- metal photodetectors," *Appl. Phys. Lett.*, vol. 88, 2006.

- [14] Chi On Chui, A.K. Okyay and K.C. Saraswat, "Effective dark current suppression with asymmetric MSM photodetectors in Group IV semiconductors," *Photonics Technology Letters, IEEE*, vol. 15; 15, pp. 1585-1587, 2003.
- [15] S. Kollakowski, U. Schade, E. H. Bottcher and D. Bimberg, "Fully passivated AR coated InP/InGaAs MSM photodetectors," *Photonics Technology Letters, IEEE*, vol. 6; 6, pp. 1324-1326, 1994.
- [16] Ching-Ting Lee and Hsin-Ying Lee, "Surface passivated function of GaAs MSM-PDs using photoelectrochemical oxidation method," *Photonics Technology Letters, IEEE*, vol. 17; 17, pp. 462-464, 2005.
- [17] S. Kollakowski, U. Schade, E. H. Bottcher, D. Kuhl, D. Bimberg, P. Ambree and K. Wandel, "Silicon dioxide passivation of InP/InGaAs metal-semiconductor-metal photodetectors," *Journal of Vacuum Science & Technology B (Microelectronics and Nanometer Structures)*, vol. 14, pp. 1712-18, 05. 1996.
- [18] Z. Pang, K. C. Song, P. Mascher and J. G. Simmons, "Sulfur passivation of InP/InGaAs metal-semiconductor-metal photodetectors," *J. Electrochem. Soc.*, vol. 146, pp. 1946-51, 05. 1999.
- [19] M. A. Matin and J. G. Simmons, "Polyimide passivated semitransparent In_{0.49}Ga_{0.51}P/GaAs MSM photodetector operating at 840 nm wavelength," *Microwave Opt Technol Lett*, vol. 22, pp. 241-3, 08/20. 1999.
- [20] Jungwoo Oh, S.K. Banerjee and J.C. Campbell, "Metal-germanium-metal photodetectors on heteroepitaxial Ge-on-Si with amorphous Ge Schottky barrier enhancement layers," *Photonics Technology Letters, IEEE*, vol. 16; 16, pp. 581-583, 2004.
- [21] A. Kinoshita, Y. Tsuchiya, A. Yagishita, K. Uchida and J. Koga, "Solution for high-performance schottky-source/drain MOSFETs: Schottky barrier height engineering with dopant segregation technique," in *Digest of Technical Papers*, 2004, pp. 168-9.
- [22] H. Zang, S. J. Lee, W. Y. Loh, J. Wang, K. Chua, M. B. Yu, B. J. Cho, G. Q. Lo and D. -. Kwong, "Dark-current suppression in metal-germanium-metal photodetectors through dopant-segregation in NiGe-Schottky barrier," *IEEE Electron Device Lett.*, vol. 29, pp. 161-4, 02. 2008.
- [23] Y. Ishikawa, K. Wada, D. D. Cannon, J. Liu, Hsin-Chiao Luan and L. C. Kimerling, "Strain-induced band gap shrinkage in Ge grown on Si substrate," *Appl. Phys. Lett.*, vol. 82, pp. 2044-6, 03/31. 2003.
- [24] J. Liu, J. Michel, W. Giziewicz, D. Pan, K. Wada, D. D. Cannon, S. Jongthammanurak, D. T. Danielson, L. C. Kimerling, J. Chen, F. O. Ilday, F. X. Kartner and J. Yasaitis, "High-performance, tensile-strained Ge p-i-n photodetectors on a Si platform," *Appl. Phys. Lett.*, vol. 87, pp. 103501-1, 2005.

- [25] Kah Wee Ang, Ming Bin Yu, Shi Yang Zhu, Khai Tze Chua, Guo Qiang Lo and Dim Lee Kwong, "Novel NiGe MSM Photodetector Featuring Asymmetrical Schottky Barriers Using Sulfur Co-Implantation and Segregation," *Electron Device Letters, IEEE*, vol. 29; 29, pp. 708-710, 2008.
- [26] H. C. Lee and B. Van Zeghbroeck, "A novel high-speed silicon MSM photodetector operating at 830 nm wavelength," *IEEE Electron Device Lett.*, vol. 16, pp. 175-7, 05. 1995.
- [27] J. Y. L. Ho and K. S. Wong, "Bandwidth enhancement in silicon metal-semiconductor-metal photodetector by trench formation," *IEEE Photonics Technology Letters*, vol. 8, pp. 1064-6, 08. 1996.
- [28] Li-Hong Lai, Tien-Chang Chang, Yen-Ann Chen, Wen-Chin Tsay and Jyh-Wong Hong, "Characteristics of MSM photodetectors with trench electrodes on p-type Si wafer," *IEEE Trans. Electron Devices*, vol. 45, pp. 2018-23, 1998.
- [29] D. Buca, S. Winnerl, S. Lenk, S. Mantl and C. Buchal, "Metal-germanium-metal ultrafast infrared detectors," *J. Appl. Phys.*, vol. 92, pp. 7599-7605, 2002.
- [30] L. Colace, G. Masini, F. Galluzzi, G. Assanto, G. Capellini, L. Di Gaspare, E. Palange and F. Evangelisti, "Metal-semiconductor-metal near-infrared light detector based on epitaxial Ge/Si," *Appl. Phys. Lett.*, vol. 72, pp. 3175-7, 06/15. 1998.
- [31] G. Masini, L. Colace, F. Galluzzi and G. Assanto, "Advances in the field of poly-Ge on Si near infrared photodetectors," *Materials Science and Engineering B*, vol. 69-70, pp. 257-260, 1/14. 2000.
- [32] L. Colace, G. Masini and G. Assanto, "Ge-on-Si approaches to the detection of near-infrared light," *IEEE J. Quant. Electron.*, vol. 35, pp. 1843-52, 12. 1999.
- [33] G. Masini, L. Colace and G. Assanto, "2.5 gbit/s polycrystalline germanium-on-silicon photodetector operating from 1.3 to 1.55 μm ," *Appl. Phys. Lett.*, vol. 82, pp. 2524-6, 04/14. 2003.
- [34] R. P. MacDonald, N. G. Tarr, B. A. Syrett, S. A. Boothroyd and J. Chrostowski, "MSM photodetector fabricated on polycrystalline silicon," *IEEE Photonics Technology Letters*, vol. 11, pp. 108-10, 01. 1999.
- [35] Kah-Wee Ang, Shi-Yang Zhu, Jian Wang, Khai-Tze Chua, Ming-Bin Yu, Guo-Qiang Lo and Dim-Lee Kwong, "Novel Silicon-Carbon (Si:C) Schottky Barrier Enhancement Layer for Dark-Current Suppression in Ge-on-SOI MSM Photodetectors," *Electron Device Letters, IEEE*, vol. 29; 29, pp. 704-707, 2008.
- [36] L. Vivien, M. Rouviere, J. -. Fedeli, D. Marris-Morini, J. -. Damlencourt, J. Mangeney, P. Crozat, L. El Melhaoui, E. Cassan, X. Le Roux, D. Pascal and S. Laval, "High speed and high responsivity germanium photodetector integrated in a silicon-on-insulator microwaveguide," *Optics Express*, vol. 15, pp. 9843-8, 07/23. 2007.

- [37] G. Harbeke, L. Krausbauer, E. F. Steigmeier, A. E. Widmer, H. F. Kappert and G. Neugebauer, "Growth and Physical Properties of LPCVD Polycrystalline Silicon Films," *J. Electrochem. Soc.*, vol. 131, pp. 675-682, March 1984. 1984.
- [38] D. Dimova-Malinovska, O. Angelov, M. Kamenova, M. Sendova-Vassileva and A. Vaseashta, "Polycrystalline silicon thin films obtained by metal-induced crystallization," *J. Mater. Sci. : Mater. Electron.*, vol. 14, pp. 747-748, 10/01. 2003.
- [39] K. A. Jackson and W. Schröter. (2000, Jun 7, 2007). *Handbook of Semiconductor Technology*.
- [40] T. I. Kamins, *Polycrystalline Silicon for Integrated Circuits and Displays*. ,2nd ed. ed.Boston : Kluwer Academic Publishers, c1998.,
- [41] Y. (. Liu, "Polysilicon metal-semiconductor-metal photodetectors for 1550 nm light," pp. 83, 2004.
- [42] R. A. Street, *Hydrogenated Amorphous Silicon*. Cambridge, United Kingdome: Cambridge University Press, 1991, pp. 417.
- [43] D. Monroe and M. A. Kastner, "Exactly exponential band tail in a glassy semiconductor," *Phys. Rev. B*, vol. 33, pp. 8881, 06/15. 1986.
- [44] R. Konenkamp "Transport in a-Si:H and Its Alloys," *Photoelectric Properties and Applications of Low-Mobility Semiconductors*, pp. 21-39, 2000.
- [45] A. J. Lewis, G. A. N. Connell, W. Paul, J. R. Pawlik and R. J. Temkin, "Hydrogen incorporation in amorphous germanium," in *International Conference on Tetrahedrally Bonded Amorphous Semiconductors*, 1974, pp. 27-32.
- [46] G. A. N. Connell and J. R. Pawlik, "Use of hydrogenation in structural and electronic studies of gap states in amorphous germanium," *Physical Review B (Solid State)*, vol. 13, pp. 787-804, 01/15. 1976.
- [47] G. Myburg, W. E. Meyer, F. D. Auret, H. Burger, W. O. Barnard and S. A. Goodman, "Fermi level pinning by metal schottky contacts on n type GaAs," in *1st International Conference on Materials for Microelectronics*, 1998, pp. 1269-72.
- [48] L. Magafas, N. Georgoulas and A. Thanailakis, "Influence of metal work function on electrical properties of metal/a-SiC:H Schottky diodes," *Microelectron. J.*, vol. 28, pp. 107-114, 1997.
- [49] C. K. Tan, A. Abdul Aziz and F. K. Yam, "Schottky barrier properties of various metal (Zr, Ti, Cr, Pt) contact on p-GaN revealed from I-V-T measurement," *Appl. Surf. Sci.*, vol. 252, pp. 5930-5935, 2006.

- [50] S.S. Islam, *Semiconductor Physics and Devices*. Oxford university press, 2006, pp. 564.
- [51] S. M. Sze , *Physics of Semiconductor Devices*. New York : Wiley-Interscience, [1969],
- [52] M. P. Lepselter and S. M. Sze, "Silicon Schottky, barrier diode with near-ideal I-V characteristics," *Bell System Technical Journal*, vol. 47, pp. 195-208, 02. 1968.
- [53] B. G. Streetman, *Solid State Electronic Devices*. ,2d ed. ed.Englewood Cliffs, N.J. : Prentice-Hall, 1980.,
- [54] S. M. Sze, D. J. Coleman Jr. and A. Loya, "Current transport in metal-semiconductor-metal (MSM) structures," *Solid-State Electronics*, vol. 14, pp. 1209-1218, 12. 1971.
- [55] S. Averine, Y. C. Chan and Y. L. Lam, "Evaluation of Schottky contact parameters in metal-semiconductor-metal photodiode structures," *Appl. Phys. Lett.*, vol. 77, pp. 274-6, 07/10. 2000.
- [56] J. B. D. Soole and H. Schumacher, "InGaAs metal-semiconductor-metal photodetectors for long wavelength optical communications," *Quantum Electronics, IEEE Journal of*, vol. 27, pp. 737-752, 1991.
- [57] S. V. Averine, Y. C. Chan and Y. L. Lam, "Optimization of high-speed MSM-photodiode structures," in *Optoelectronic and Microelectronic Materials and Devices, 2000. COMMAD 2000. Proceedings Conference on*, 2000, pp. 515-518.
- [58] K. Wasa, M. Kitabatake and H. Adachi, *Thin Film Materials Technology Sputtering of Compound Materials*. Norwich, NY : Heidelberg : William Andrew Pub. ; Springer, c2004.,
- [59] J. E. Davey, R. J. Tiernan, T. Pankey and M. D. Montgomery, "The effect of vacuum-evaporation parameters on the structural, electrical and optical properties of thin germanium films," *Solid-State Electronics*, vol. 6, pp. 205-212, 6. 1963.
- [60] B. W. Sloope and C. O. Tiller, "Electrical properties of epitaxial Ge films deposited on (111) CaF₂ substrates," *J. Appl. Phys.*, vol. 38, pp. 140-148, 01. 1967.
- [61] K. E. Haq. Deposition of germanium films by sputtering. *112(5)*,
- [62] K.B. Sundaram , B.K. Garside, "Controlled Doping of rf Sputtered Germanium Films," vol. 34, pp. 117, 1984.
- [63] Y. Yang, X. Mao, H. Li, Z. Zhou, S. Jiang, X. Wu, S. Huang and P. Zhang, "Growth of germanium crystal films on amorphous silicon by sputter deposition," *Physica E: Low-Dimensional Systems and Nanostructures*, vol. 8, pp. 72-76, 7. 2000.
- [64] G. Wallis, E. E. Pittelli and J. Pantano, "Electrical properties of sputtered germanium films," *Thin Solid Films*, vol. 4, pp. 309-17, 11. 1969.

- [65] H. Min, S. Ueda, M. Kumeda and T. Shimizu, "Relation between ESR and hydrogen in magnetron-sputtered a-Ge:H," *Japanese Journal of Applied Physics, Part 2 (Letters)*, vol. 36, pp. 82-4, 02/01. 1997.
- [66] T. Drusedau and B. Schroder, "Optimization of process parameters for the deposition of improved a-Ge:H by dc magnetron sputtering," *J. Appl. Phys.*, vol. 75, pp. 2864-75, 03/15. 1994.
- [67] R. P. MacDonald, "Components for a low-cost integrated silicon optical receiver," pp. 199, 2002.
- [68] D. L. Rogers, "MESFET compatible IMSM detectors," in *Conference Edition*, 1987, pp. 116-20.
- [69] L. S. Yu, L. Jia, D. Qiao, S. S. Lau, J. Li, J. Y. Lin and H. X. Jiang, "The origins of leaky characteristics of Schottky diodes on p-GaN," *Electron Devices, IEEE Transactions on*, vol. 50; 50, pp. 292-296, 2003.
- [70] M. Li and W. A. Anderson, "Si-based metal-semiconductor-metal photodetectors with various design modifications," *Solid State Electronics*, vol. 51, pp. 72-79,
- [71] M. Sahin, H. Durmus and R. Kaplan, "Current-voltage analysis of a-Si:H Schottky diodes," *Appl. Surf. Sci.*, vol. 252, pp. 6269-74, 07/15. 2006.
- [72] E. H. Rhoderick and R. H. Williams, *Metal-Semiconductor Contacts*, 2nd ed. ed. Oxford [England] : New York : Clarendon Press ; Oxford University Press, 1988.,
- [73] F. Fajardo and I. Chambouleyron, "Hydrogenated amorphous germanium schottky barrier diodes," in *Seventh Latin-American Symposium on Surface Science (SLAFFS7-CIACSA1)*, 1993, pp. 347-8.
- [74] S. M. M. Coelho, F. D. Auret, P. J. J. van Rensberg, C. Nyamhere, J. M. Nel and M. Hayes, "IV and CV measurements of Schottky diodes deposited on Ge by electron beam and sputter deposition," *Physica Status Solidi C*, vol. 5, pp. 626-9, 02. 2008.
- [75] C. J. Fang, K. J. Gruntz, L. Ley, M. Cardona, F. J. Demond, G. Muller and S. Kalbitzer, "The hydrogen content of a-ge:H and a-si:H as determined by IR spectroscopy, gas evolution and nuclear reaction techniques," in *Proceedings of the Eighth International Conference on Amorphous and Liquid Semiconductors*, 1980, pp. 255-60.